IFS #617

Shear Flow Generation from the Interaction of Neoclassical and Drift Wave Transport Processes

X.N. Su, P.N. Yushmanov, J.Q. Dong, and W. Horton
Institute for Fusion Studies
The University of Texas at Austin
Austin, Texas 78712

Abstract

Self-consistent shear flow generation from the interaction of neoclassical and drift wave turbulence effects is investigated. The neoclassical poloidal flow damping is shown to compete with the plasma flow generation driven through the divergence of the Reynolds stress. When there is no external driving force except for the free energy released from toroidal shear flow, the turbulent fluctuations occur as a transient pulse which takes the system along an equilibrium path to a relaxed state. External torques, such as parallel neutral beam injection, are needed to maintain significant fluctuation levels. For a system driven by a fixed ion temperature gradient, although linearly the poloidal shear flow generated substantially reduces the growth rate, the simulation results show that a sequence of nonlinear pulses occurs that eventually build the fluctuations up to a level that is not significantly affected by the poloidal flow. In this new, highly nonlinear state the transport is intermittent, with high fluxes occurring through a sequence of pulses of duration $100\, L_n/c_s$ for typical parameters.

I Introduction

Recently, the effects of background shear flow on turbulent transport have been subject to intensive studies.[1–7] These studies are motivated by recent tokamak experimental observations showing significant levels of radially sheared toroidal flow in neutral-beam heated discharge and a sharp increase in the poloidal shear flow in the edge region of tokamaks which occurs simultaneously with the decrease of the fluctuation level. It is believed that the generation of background poloidal shear flow may be responsible for the decrease in the fluctuation level at the plasma edge and for the improvement of plasma confinement, or the L-H transition.

Generally, it is known that a perpendicular shear flow has a strong stabilizing effect,[8–11] by introducing a radial asymmetry in the eigenfunction which causes modes with different radial wavenumbers to couple and a parallel shear flow can drive instability by releasing free energy.[8–11] In many earlier works the effects of background perpendicular and parallel shear flow on turbulence have been studied either separately or with fixed background flow. For purely toroidal flows, Waelbroeck *et al.*[11] have shown that the perpendicular component of shear flow can overcome the destabilizing effect of the parallel component for large flow shear. However recent studies[3,4] suggest that the background poloidal and toroidal flow will be modified through the Reynolds stress when interaction or coupling between turbulent fluctuation and background mean flow becomes strong. Therefore the studies of the combined effect of toroidal and poloidal shear *in self-consistently evolving background flow* are important to understand the development of fluctuations and plasma transport.

Neoclassical theory has shown that plasma flow in nonuniform toroidal magnetic field will experience poloidal flow damping due to the magnetic pumping effect,[12–17] or the so-called neoclassical effect. The effect arises due to the fact that when the plasma rotates from the weak to strong toroidal magnetic field, the cross-section of the flux tube becomes

small because of the flux preservation. Since the collision frequency is finite, the rotation heats the plasma and leads to an irreversible transformation of the kinetic energy of rotation into thermal energy. In a turbulent plasma, therefore, the neoclassical effect competes with the effect of turbulent fluctuation which tends to drive background mean plasma flow and significantly affects the generation and development of mean plasma shear flow.

In this work we focus on the shear flow generation with the interaction of drift wave turbulence effect and the neoclassical effect. We study the two turbulence models, one is parallel flow shear $u'_{\parallel}$ driven instability model and the other is the η_i instability model. The $u'_{\parallel}$ driven mode, as we know, drives the instability by releasing free energy stored in sheared parallel velocity profile. As the modes grow, the perpendicular shear flow will be driven through the divergence of the Reynolds stress. This shear flow then suppresses the turbulence. In the meanwhile the magnetic pumping effect causes the damping of the mean poloidal flow. From the point of view of energy, the free energy released from toroidal shear flow first goes to drive turbulence, then part of energy goes to the poloidal flow through Reynolds stress. The poloidal flow energy is subject to loss from the plasma heating due to neoclassical viscosity force (or magnetic pumping). Therefore in a closed system, that is, a system without external driving forces, the plasma flow which starts in an unstable state always relaxes to a stable state along an equilibrium path. During the transition the fluctuations grow up driven by the free energy in the sheared flow and then slowly decays (as a power law in time) as a new stable state is approached.

To maintain significant fluctuation levels, it is necessary to have external driving forces. The two kinds of external forces are used. One is parallel neutral beam injection which drives the background parallel shear flow. The other is the ion temperature gradient driving force which directly drives the fluctuations. The grown-up turbulent fluctuations then drive background poloidal and toroidal flow through the forces arising from the turbulent transport of plasma momentum. The saturation can be achieved when the external forces are balanced

by neoclassical effect and the viscosity force acting on the fluctuations.

This work is organized as follows. Section II gives an introduction to the neoclassical flow. The basic derivation of self-consistent background flow evolution equations with neoclassical effect and drift-acoustic wave turbulence effect, and the equations of the mode evolution are also given in this section. In Sec. III, linear stability analysis is briefly presented. In Sec. IV, we show and discuss the results of the 2-D numerical simulations. Summary and conclusions are given in Sec. V.

II Neoclassical Flows

First order plasma flow $\mathbf{v}$ that lies within a magnetic surface is determined in the toroidally symmetric confinement systems by two magnetic surface functions

$$u_{\parallel} = \frac{\langle \mathbf{v} \cdot \mathbf{B} \rangle}{B_0} \qquad u_{\perp} = \frac{B_0}{2\pi R_0 B_P} \left\langle \mathbf{v} \cdot \left(\frac{\nabla\psi \times \mathbf{B}}{B^2} \right) \right\rangle \tag{1}$$

where $\mathbf{B} = R_0 B_T \nabla\phi + (1/2\pi)(\nabla\phi \times \nabla\psi)$, B_P and B_T are poloidal and toroidal magnetic field components, respectively, $B_0 = \langle B^2 \rangle^{1/2} = \langle B_P^2 + B_T^2 \rangle^{1/2}$, ψ is poloidal magnetic flux, ϕ, θ are toroidal and poloidal angles and angle brackets means averaging over magnetic surface

$$\langle A \rangle = \frac{\int \frac{A d\theta}{\mathbf{B} \cdot \nabla\theta}}{\int \frac{d\theta}{\mathbf{B} \cdot \nabla\theta}} .$$

The mean flow velocity $\mathbf{v}$ can be written in the following vector form[12]

$$\mathbf{v} = \frac{\mathbf{B}}{B_0} \left(u_{\parallel} - \frac{B_T}{B_P} u_{\perp} \right) + u_{\perp} \frac{B_0}{R_0 B_P} R^2 \nabla\phi \, . \tag{2}$$

In Eq. (2) the first term represents incompressible plasma flow along magnetic field lines and the second one describes the rigid body rotation of a magnetic surface. Rigid body rotation (the second term in Eq. (2)) does not contribute to the lowest order viscosity, therefore standard neoclassical viscosity force can depend only on the combination $u_{\parallel} - (B_T/B_P)u_{\perp}$.

The connection of the perpendicular flow velocity $u_\perp$ defined in Eq. (1) with radial electric field E_r is provided by the radial force balance equation which gives

$$u_\perp = -(2\pi\, B_0 c/R_0\, B_p) \left\langle R^2\, B_p^2/B^2 \right\rangle \left(\frac{d\Phi}{d\psi} + \frac{1}{en}\frac{dP}{d\psi} \right)$$

where E_r is determined by electrostatic potential $\Phi(\psi)$ and $P(\psi)$ is the ion pressure. The velocity $u_\perp$ is defined such that positive E_r gives positive $u_\perp$ which is rotation in the ion diamagnetic direction.

Plasma rotation equations in toroidally symmetric systems describe the time evolution of surface functions $u_\parallel$ and $u_\perp$. We can obtain these equations from momentum balance equation following standard procedure described, for example, in Hassam and Kulsrud,[13] Hirshman,[14] and Ware and Wiley[15]

$$nm(1+2\hat{q}^2)\frac{\partial u_\perp}{\partial t} = -F_\perp^R - F_\sim^R - F^{mc} - F_\perp^a \,, \tag{3}$$

$$nm\frac{\partial u_\parallel}{\partial t} = \frac{B_P}{B_T}F^{mc} - F_\parallel^R - F_\parallel^a \,, \tag{4}$$

where the standard toroidal geometry enhancement factor is

$$2\hat{q}^2 = \left(\frac{B_T}{B_P}\right)^2 \left(1 - \frac{1}{\langle R^2\rangle \langle R^{-2}\rangle}\right) \approx 2q^2 \,,$$

and the last reduction is for large aspect ratio. In deriving Eqs. (3) and (4) we take the plasma velocity as $\mathbf{v} + \tilde{\mathbf{v}}$ with the mean velocity $\mathbf{v}$ given by Eq. (2) in terms of $u_\perp$ and $u_\parallel$ and $\tilde{\mathbf{v}}$ to be determined by the fluctuation dynamics. Forces marked by index R represent momentum generation produced by fluctuation-related Reynolds stress

$$F_\parallel^R = \left\langle nm\frac{\mathbf{B}}{B_0}\cdot((\tilde{\mathbf{v}}\cdot\boldsymbol{\nabla})\tilde{\mathbf{v}}) \right\rangle \,; \tag{5}$$

$$F_\perp^R = \left\langle nm\frac{B_0(\boldsymbol{\nabla}\psi\times\mathbf{B})}{2\pi R_0 B_P B^2}\cdot((\tilde{\mathbf{v}}\cdot\boldsymbol{\nabla})\tilde{\mathbf{v}}) \right\rangle \,; \tag{6}$$

$$F_\sim^R = \left\langle nm\frac{B_T}{B_P}\left(\frac{B_0^2}{B^2}-1\right)\frac{\mathbf{B}}{B_0}\cdot((\tilde{\mathbf{v}}\cdot\boldsymbol{\nabla})\tilde{\mathbf{v}}) \right\rangle \,; \tag{7}$$

and

$$F^{nc} = -\frac{B_T}{B_0 B_P}\left\langle B^2(\mathbf{B}\cdot\boldsymbol{\nabla})\frac{P_\parallel - P_\perp}{2B^2}\right\rangle \tag{8}$$

describes neoclassical viscosity force emerging when plasma is pushed along the nonuniform magnetic field (the magnetic pumping effect) and terms marked by index a represent flow damping due to the breakdown of toroidal symmetry of the system that is always present in real devices

$$F^a_\perp = \left\langle \left[\frac{B_0\boldsymbol{\nabla}\psi\times\mathbf{B}}{2\pi R_0 B_P B^2} + \frac{B_T}{B_P}\left(\frac{B_0^2}{B^2}-1\right)\frac{\mathbf{B}}{B_0}\right]\cdot\mathbf{F}^a\right\rangle , \tag{9}$$

$$F^a_\parallel = \left\langle \frac{\mathbf{B}}{B_0}\cdot\mathbf{F}^a\right\rangle . \tag{10}$$

The force $\mathbf{F}^a$ can describe the effect of toroidal ripples or charge exchange collisions of ions with neutral gas.

According to Ref. 12 neoclassical viscosity is proportional to poloidal rotation velocity and can be written in the form

$$F^{nc} = -3\mu^{nc}\frac{B_T}{B_0^2 B_P}\left\langle\left(\frac{(\mathbf{B}\cdot\boldsymbol{\nabla})B}{B}\right)^2\right\rangle\left(u_\parallel - \frac{B_T}{B_P}u_\perp - k_{\nu_*}\frac{c}{eB_P}\frac{dT_i}{dr}\right) , \tag{11}$$

where μ^{nc} is the neoclassical viscosity coefficient, that for the standard neoclassical assumptions of low rotation velocity $u \ll c_s$, scales as[12,16]

$$\mu^{nc} \approx R_0 q\frac{nmV_{th}\nu_*}{1+\nu_*}\frac{1}{1+\epsilon^{3/2}\nu_*} , \tag{12}$$

where $\nu_* = qR_0\nu/V_{th}\epsilon^{3/2}$, ν is ion collision frequency, $\epsilon = r/R_0$ is inverse aspect ratio, V_{th} is thermal velocity of the plasma component and the coefficient k_{ν_*} describes the relative effect of parallel heat flux on the longitudinal viscosity,[17] which has following values:

$$\begin{aligned} k_{\nu_*} &= 1.17 \quad \text{for} \quad \nu_* \ll 1 \\ k_{\nu_*} &= -0.5 \quad \text{for} \quad 1 \ll \nu_* \ll \epsilon^{-3/2} \\ k_{\nu_*} &= -2.1 \quad \text{for} \quad \nu_* \gg \epsilon^{-3/2} . \end{aligned} \tag{13}$$

Here we do not want to specify any particular model of a toroidally asymmetric process that produces the nonambipolar forces $F_\perp^a$ and $F_\parallel^a$. We use somewhat heuristic forms of the forces for the description of the process:

$$F_\perp^a = nm\nu_\perp^a(u_\perp - u_\perp^a) \ , \tag{14}$$

$$F_\parallel^a = nm\nu_\parallel^a(u_\parallel - u_\parallel^a) \ . \tag{15}$$

The forms of the nonambipolar forces given in Eqs. (14) and (15) may describe the process such as charge exchange with neutral beams (or beam injection) that can be derived from hydrodynamical equations.

Substituting Eqs. (11)–(15) into Eqs. (3) and (4), we obtain the following equation for mean plasma rotation in toroidally symmetric system

$$(1+2q^2)\frac{\partial u_\perp}{\partial t} = -\nu^{nc}\left(u_\perp - S_0 u_\parallel + u^{nc}\right) - \nu_\perp^a(u_\perp - u_\perp^a) - \frac{\partial}{\partial x}\left\langle \tilde{v}_x\tilde{v}_\perp\right\rangle - 2q\left\langle \cos\theta\frac{\partial}{\partial x}(\tilde{v}_x\tilde{v}_\parallel)\right\rangle \ , \tag{16}$$

$$\frac{\partial u_\parallel}{\partial t} = -\nu^{nc}S_0\left(S_0 u_\parallel - u_\perp - u^{nc}\right) - \nu_\parallel^a(u_\parallel - u_\parallel^a) - \frac{\partial}{\partial x}\left\langle \tilde{v}_x\tilde{v}_\parallel\right\rangle \ , \tag{17}$$

where

$$\nu^{nc} = \frac{3\mu^{nc}}{nm}\frac{B_T^2}{B_P^2B_0^2}\left\langle\left(\frac{(\mathbf{B}\cdot\boldsymbol{\nabla})B}{B}\right)^2\right\rangle \approx \frac{3}{2}\frac{B_T^2}{B_P^2}\frac{\sqrt{\epsilon}}{1+\nu_*}\left(\frac{\nu L_n}{c_s}\right) \ , \tag{18}$$

$$S_0 = \frac{B_P}{B_T} \quad \text{and} \quad u^{nc} = k_{\nu_*}\frac{c}{eB_T}\frac{dT_i}{dr}\left(\frac{L_n}{\rho_s c_s}\right) \ . \tag{19}$$

In writing Eqs. (16) and (17) we reduce the cross-field gradient by $\partial/\partial\psi = (2\pi RB_p)^{-1}\partial/\partial x$ and use the high aspect ratio approximation ($\epsilon \ll 1$).

The first terms on the right-hand side of Eqs. (16) and (17) give the neoclassical damping of the poloidal rotation velocity $u_\theta = u_\perp - S_0 u_\parallel$ to the equilibrium value $u_\theta = -u^{nc}$ given in Eq. (19). This equilibrium poloidal velocity determined by the ion temperature gradient is in the ion diamagnetic direction for $\nu_* > 1$ when $k_{\nu_*} < 0$ and in the electron direction

for $\nu_* < 1$ when $k_{\nu_*} > 0$. The toroidal velocity $u_\phi = u_\parallel + S_0 u_\perp$ is not damped by the neoclassical term ν^{nc} due to the toroidal symmetry assumed in calculating the F^{nc} force in Eq. (11).

The perpendicular and parallel mean flows are thus determined by the competition between the neoclassical transport coefficients ν^{nc}, $\nu^a_\perp$, $\nu^a_\parallel$ and the turbulent (Reynolds) flow tensors given by $\pi_{x\perp} = \langle \tilde{v}_x \tilde{v}_\perp \rangle$ and $\pi_{x\parallel} = \left\langle \tilde{v}_x \tilde{v}_\parallel \right\rangle$.

The dynamical equations for the fluctuation fields $\tilde{\varphi}$ and $\tilde{v}_\parallel$ in the local slab geometry are taken as[6,9,18]

$$(1-\nabla_\perp^2)\frac{\partial \tilde{\varphi}}{\partial t} + v_d \frac{\partial \tilde{\varphi}}{\partial y} + \left(\frac{\partial^2 u_\perp}{\partial x^2} + (u_\perp + S_0 u_\parallel)(1-\nabla_\perp^2) \right) \frac{\partial \tilde{\varphi}}{\partial y} - \left[\tilde{\varphi} \quad , \nabla_\perp^2 \tilde{\varphi} \right] = -\nabla_\parallel \tilde{v}_\parallel - \mu_\perp \nabla_\perp^4 \tilde{\varphi} \, , \tag{20}$$

$$\frac{\partial \tilde{v}_\parallel}{\partial t} + (u_\perp + S_0 u_\parallel)\frac{\partial \tilde{v}_\parallel}{\partial y} - \frac{\partial u_\parallel}{\partial x}\frac{\partial \tilde{\varphi}}{\partial y} + \left[\tilde{\varphi} \quad , \tilde{v}_\parallel \right] = -\nabla_\parallel \tilde{\varphi} + \mu_\perp \nabla_\perp^2 \tilde{v}_\parallel \, , \tag{21}$$

where

$$\begin{aligned} \boldsymbol{\nabla}_\perp &= \hat{\mathbf{x}} \frac{\partial}{\partial x} + \hat{\mathbf{y}} \frac{\partial}{\partial y} \, , \\ \nabla_\parallel &= \frac{\partial}{\partial z} + (L_n/\rho_s) S_0 \frac{\partial}{\partial y} \, , \\ [f \, , \, g] &= \frac{\partial f}{\partial x}\frac{\partial g}{\partial y} - \frac{\partial f}{\partial y}\frac{\partial g}{\partial x} \, , \end{aligned} \tag{22}$$

and $u_\perp = u_\perp(x,t)$ and $u_\parallel = u_\parallel(x,t)$ are the background perpendicular rotation and parallel flow velocity field given by Eqs. (16) and (17), respectively.

In Eqs. (20) and (21), $\mu_\perp$ is the dissipation coefficient from collisional ion viscosity and $S_0 = B_y/B_0$ ($\simeq B_P/B_T$) is the magnetic tilting angle.

The usual drift wave scalings are used in the non-dimensional variables in above equations:

$$\begin{aligned} &x' \, , \; y' = x/\rho_s \, , \; y/\rho_s \, , \quad z' = z/L_n \, ; \\ &t' = c_s t/L_n \, ; \end{aligned} \tag{23}$$

$$\varphi' = \left(\frac{L_n}{\rho_s}\right)\left(\frac{e\Phi}{T_e}\right) \ ;$$

and all the velocities, $u_\perp$, $u_\parallel$, $\tilde{v}_\parallel$ and $\tilde{\mathbf{v}}_\perp$ $(= (\rho_s c_s/L_n)\mathbf{b}\times\boldsymbol{\nabla}_\perp\tilde{\varphi})$, are in units of the electron diamagnetic drift velocity $v_{de} = \rho_s c_s/L_n$.

Equations (20) and (21) together with Eqs. (16) and (17) are the basic model equations used in our simulations with the results given in Sec. IV. In the following sections we use the dimensionless variables and omit the primes. These nonlinear coupled equations for the neoclassical evolution of the mean flows and the dynamics of the fluctuations form a new hybrid neoclassical- drift wave turbulence model for the toroidal plasma.

The total energy E is dissipated only by the small dissipation from perpendicular viscosity $\mu_\perp$ and the neoclassical drags due to collisional relaxations of the anisotropics driven by the rotation. The fluctuations transfer the background flow energies (E_{bg1}) and (E_{bg2}) through the two (Reynolds) tensors. So we find it useful to define and study the four energy components obtained by dividing the poloidal or $\mathbf{E}\times\mathbf{B}$ flow and the toroidal or parallel flow into their background (bg) mean flow components and into their fluctuating (fl) kinetic components. The definition of these four components are as follows:

$$E_{bg,1} = \frac{1}{2}\int_V (1+2q^2)u_\perp^2\frac{dV}{L_xL_y} \ , \tag{24}$$

$$E_{fl,1} = \frac{1}{2}\int_V (\tilde{\varphi}^2 + (\nabla_\perp\tilde{\varphi})^2)\frac{dV}{L_xL_y} \ , \tag{25}$$

$$E_{bg,2} = \frac{1}{2}\int_V u_\parallel^2\frac{dV}{L_xL_y} \ , \tag{26}$$

$$E_{fl,2} = \frac{1}{2}\int_V \tilde{v}_\parallel^2\frac{dV}{L_xL_y} \ . \tag{27}$$

The Reynolds tensors are defined by

$$\pi_{x\perp} = \langle\tilde{v}_x\tilde{v}_\perp\rangle = -\int\frac{dy}{L_y}\frac{\partial\tilde{\varphi}}{\partial x}\frac{\partial\tilde{\varphi}}{\partial y} = \mathrm{Im}\sum_{k_y} k_y\tilde{\varphi}^*_{k_y}\frac{\partial\tilde{\varphi}_{k_y}}{\partial x} \ , \tag{28}$$

$$\pi_{x\|} = \left\langle \widetilde{v}_x \widetilde{v}_\| \right\rangle = -\int \frac{dy}{L_y} \frac{\partial \widetilde{\varphi}}{\partial y} \widetilde{v}_\| = \mathrm{Im} \sum_{k_y} k_y \widetilde{\varphi}^*_{k_y} \widetilde{v}_{\| k_y} \ . \tag{29}$$

The two Reynolds stress tensors control the flow of energy between the background and fluctuating flow components. The energy conservation laws can be written as

$$\frac{dE_{bg,1}}{dt} = -\nu^{nc} \int u_\perp (u_\perp - S_0 u_\| + u^{nc}) \frac{dx}{L_x} - \nu^a_\perp \int u_\perp (u_\perp - u^a_\perp) \frac{dx}{L_x} - \int u_\perp \frac{\partial \pi_{x\perp}}{\partial x} \frac{dx}{L_x} \ , \tag{30}$$

$$\frac{dE_{fl,1}}{dt} = \int u_\perp \frac{\partial \pi_{x\perp}}{\partial x} \frac{dx}{L_x} - \int_V \widetilde{\varphi} \nabla_\| \widetilde{v}_\| \frac{dV}{L_x L_y} - \mu_\perp \int_V (\nabla^2_\perp \widetilde{\varphi})^2 \frac{dV}{L_x L_y} \ , \tag{31}$$

$$\frac{dE_{bg,2}}{dt} = \nu^{nc} \int u_\| S_0 (u_\perp - S_0 u_\| + u^{nc}) \frac{dx}{L_x} - \nu^a_\| \int u_\| (u_\| - u^a_\|) \frac{dx}{L_x} - \int u_\| \frac{\partial \pi_{x\|}}{\partial x} \frac{dx}{L_x} \ , \tag{32}$$

$$\frac{dE_{fl,2}}{dt} = \int u_\| \frac{\partial \pi_{x\|}}{\partial x} \frac{dx}{L_x} - \int_V \widetilde{v}_\| \nabla_\| \widetilde{\varphi} \frac{dV}{L_x L_y} - \mu_\perp \int_V (\nabla_\perp \widetilde{v}_\|)^2 \frac{dV}{L_x L_y} \ , \tag{33}$$

and thus the total energy conservation is

$$\begin{aligned} \frac{d}{dt} \left[\sum_{1,2} (E_{bg} + E_{fl}) \right] = & -\mu_\perp \int_V (\nabla^2_\perp \widetilde{\varphi})^2 \frac{dV}{L_x L_y} - \mu_\perp \int_V (\nabla_\perp \widetilde{v}_\|)^2 \frac{dV}{L_x L_y} \\ & -\nu^{nc} \int \left[(u_\perp - S_0 u_\|)(u_\perp - S_0 u_\| + u^{nc}) \right] \frac{dx}{L_x} \\ & -\nu^a_\perp \int u_\perp (u_\perp - u^a_\perp) \frac{dx}{L_x} - \nu^a_\| \int_V u_\| (u_\| - u^a_\|) \frac{dx}{L_x} \ . \end{aligned} \tag{34}$$

To write Eqs. (30)–(34), we have noticed that

$$\begin{aligned} \int u_\perp \frac{\partial \pi_{x\perp}}{\partial x} \frac{dx}{L_x} &= -\int \frac{\partial u_\perp}{\partial x} \pi_{x\perp} \frac{dx}{L_x} \ , \\ \int u_\| \frac{\partial \pi_{x\|}}{\partial x} \frac{dx}{L_x} &= -\int \frac{\partial u_\|}{\partial x} \pi_{x\|} \frac{dx}{L_x} \ . \end{aligned} \tag{35}$$

These relations presented in Eqs. (30)–(34) also show that $(E_{bg} + E_{fl})_{1,2}$ are conserved within the small scale dissipation $\mu_\perp$ and the large scale neoclassical field. Equations (30), (32) and (34) also indicate that when $\nu^a_\perp = \nu^a_\| = 0$ the background mean flow possesses two equilibrium states defined by $u_\perp - S_0 u_\| = 0$ and $u_\perp - S_0 u_\| + u^{nc} = 0$, and the effect of neoclassical damping is to relax the flow to either of the states. The relaxation time is determined by $(1/\nu^{nc})(L_n/c_s)$. For $\nu_* \simeq 1$ the relaxation time is $\simeq qR_0/V_{th}$ which is tens of microseconds. For $\nu_* \lesssim 1$ we have the dimensionless parameter $\nu^{nc} \simeq (3/2)(\epsilon_n q)(T_i/T_e)^{1/2} \nu_* \simeq \nu_*$.

III Linear Instability

We now examine the linear stability of the parallel shear flow driven mode in the magnetic shearless system based on the model equations (20) and (21). Considering the linear modes have the wave form of $\tilde{\varphi} = \tilde{\varphi}(x)\exp[i(k_y y - \omega t)]+$ c.c., we can derive the eigenmode equations by linearizing Eqs. (20) and (21) as

$$\frac{\partial^2\tilde{\varphi}}{\partial x^2} + \left[-(1+k_y^2) + \frac{\omega_* + k_y u_\perp''(x)}{\omega - k_y u_\perp(x) - k_\parallel u_\parallel(x)} - \frac{k_\parallel(k_y u_\parallel'(x) - k_\parallel)}{[\omega - k_y u_\perp(x) - k_\parallel u_\parallel(x)]^2}\right]\tilde{\varphi} = 0\ , \qquad (36)$$

where $\omega_* = k_y v_d = L_n\omega_{*e}/c_s$ is dimensionless diamagnetic rotation. In the quasilinear evolution the flow profiles $u_\perp(x,t), u_\parallel(x,t)$ take on complicated structures. For profiles with weak $u_\perp''$ we may expand the mean perpendicular and parallel velocity as $u_\perp(x) \simeq u_{0\perp}(0) + u_\perp' x$ and $u_\parallel(x) \simeq u_{0\parallel}(0) + u_\parallel' x$ and transform to the moving frame so that $u_{0\perp}(0) = u_{0\parallel}(0) = 0$ in the moving frame. The laboratory frame frequencies must be Doppler shifted by $k_y u_{0\perp}(0) + k_\parallel u_{0\parallel}(0)$ from those obtained in the following stability analysis. Equation (36) is then a Whittaker equation[11] with no converging mode in $-\infty \le x \le \infty$ space due to the fact that $(1+k_y^2) > 0$. However, if the expansions for $u_\perp(x)$ and $u_\parallel(x)$ are assumed to be valid only in a finite domain of x space, then the solutions which converge in the finite domain of x space are relevant and unstable under the conditions given here.

Now we first consider the mode which is well localized such that $|k_y u_\perp' + k_\parallel u_\parallel'||x| \ll |\omega|$. We can therefore obtain the lowest order eigenmode equation from Eq. (36)

$$\frac{\partial^2\tilde{\varphi}}{\partial x^2} + (A + Bx - Cx^2)\tilde{\varphi} = 0 \qquad (37)$$

where

$$A = -(1+k_y^2) + \frac{\omega_*}{\omega} - \frac{k_\parallel(k_y u_\parallel' - k_\parallel)}{\omega^2}$$
$$B = \frac{(k_y u_\perp' + k_\parallel u_\parallel')}{\omega^2}\left[\omega_* - \frac{2k_\parallel(k_y u_\parallel' - k_\parallel)}{\omega}\right] \qquad (38)$$

$$C = \frac{(k_y u'_\perp + k_\parallel u'_\parallel)^2}{\omega^3}\left[\frac{3k_\parallel(k_y u'_\parallel - k_\parallel)}{\omega} - \omega_*\right] .$$

The lowest eigenmode solution of Eq. (37) is given by

$$\tilde{\varphi}(x) = \exp[-\frac{\sqrt{C}}{2}(x - \frac{B}{2C})^2] . \tag{39}$$

For $\omega_*\omega < k_\parallel(k_y u'_\parallel - k_\parallel)$, the eigenvalue can be determined by

$$\omega = \frac{\omega_* \pm \sqrt{\omega_*^2 - 4(1+k_y^2)\left[(2/3)k_\parallel(k_y u'_\parallel - k_\parallel) - \sqrt{3k_\parallel(k_y u'_\parallel - k_\parallel)}(k_y u'_\perp + k_\parallel u'_\parallel)\right]}}{2(1+k_y^2)} \tag{40}$$

The marginal instability can be derived from Eq. (40)

$$\omega_*^2 - 4(1+k_y^2)\left[(2/3)k_\parallel(k_y u'_\parallel - k_\parallel) - \sqrt{3k_\parallel(k_y u'_\parallel - k_\parallel)}(k_y u'_\perp + k_\parallel u'_\parallel)\right] = 0 . \tag{41}$$

When the dimensionless diamagnetic rotation $\omega_* = L_n\omega_{*e}/c_s$ is small, compared with the flow shears, we obtain

$$(k_y u'_\perp + k_\parallel u'_\parallel)^2 \simeq \frac{4}{27}k_\parallel(k_y u'_\parallel - k_\parallel) . \tag{42}$$

Equation (42) describes the balance of poloidal shear flow stabilization with the parallel shear flow destabilization. For $k_\parallel = 1/qR$ the first unstable k_y is $k_y = (u'^2_\parallel - 4/27)/(qRu'_\parallel(4/27 - u'_\perp)$ and the fastest growing mode for large $|u'_\parallel|$ is $k_y = 2/qRu'_\parallel$ with $\gamma_{\max} = 2u'_\parallel/\sqrt{(qRu'_\parallel)^2 + 2qRu'_\parallel}$.

In a general case Eq. (36) has to be solved numerically to get eigenvalues ω and eigenfunctions $\tilde{\varphi}(x)$. In Figs. 1(a) and 1(b) the normalized growth rate contours are shown in $u'_\perp = (L_n/c_s)dV_E/dx$ and $u'_\parallel = (L_n/c_s)dV_\parallel/dx$ space for magnetic shearless and with magnetic shear ($k_\parallel = k_y x/L_s$ and $s = L_n/L_s$) configurations, respectively. The mode with maximum growth rate is chosen among the modes found and the growth rate is not sensitive to the boundary of the region. For the case with magnetic shear [Fig. 1(b)] the contours with higher growth rate are shown to avoid high $u'_\perp$ values which makes the stability problem complicated and it will be discussed in a separate work. The interaction of $u'_\parallel$ and η_i destabilization is studied elsewhere[9] and not considered here. In the presence of η_i and small $u'_\perp$ the stability analysis is given in Hamaguchi and Horton (1992).[6]

IV Results of Numerical Simulations

In this section we report and discuss the results of the nonlinear numerical simulations. We numerically solve Eqs. (16)–(21) using procedures described in Ref. 19. One can study the model in two cases, local and global mode cases. In the global mode case, the magnetic field in the y direction, B_y, is considered a small finite constant, so that the magnetic parameter $S_0 = B_y/B_0 = \text{const}$. For the local mode case, B_y is a function of x, so that $S(x) = B_y(x)/B_0$ depends on x, which gives a 2D model for the effect of magnetic shear. In the case of a sheared magnetic field, it is important to distinguish between single helicity simulation/theory and full 3D multihelicity simulation/theory as analyzed by Beklemishev and Horton.[20] A recent study[21] indicates that it is physically more relevant to treat B_y/B_0 as a constant in the two-dimensional case, while in three-dimensional case it is necessary to treat B_y/B_0 as a function of x since there are multiple rational surfaces with overlapping wave functions. In this work we only consider the two-dimensional case, and therefore in all of our simulation cases, we consider S_0 to be a constant.

In this work, the simulation box is taken to be $L_x = L_y = 20\pi\rho_s$, which is to represent the region of strong shear flow. We usually set initial background poloidal rotation $u_\perp(x, t = 0) = u_{\perp 0}\sin(k_1 x)$ and parallel shear flow $u_\parallel(x, t = 0) = u_{\parallel 0}\sin(k_1 x)$, where $k_1 = 2\pi/L_x$, which means in physical units a variation of $u_\parallel$ by $u_{\parallel 0}c_s(\rho_s/L_n)$ over the scale of $62\rho_s$ (typically 6 cm). The initial fluctuations of $\tilde{\varphi}$ and $\tilde{v}_\parallel$ are usually set $\tilde{\varphi} = \tilde{v}_\parallel = 0.1\exp[-(x^2 + y^2)/r_0^2)]$ or, alternatively, $0.1x\exp[-(x^2 + y^2)/r_0^2]$ with $r_0 = 6[\rho_s]$. The neoclassical flow velocity is $u^{nc} = u_0^{nc}\sin(k_1 x)$. The set of Eqs. (16)–(21) is solved in an 85×85 $k_x k_y$ space with Runge-Kutta-Verner fifth-order and sixth-order method for advancing in time.

We have tested the accuracy of the nonlinear evolution by studying energy conservation in both the two-field code with φ–$v_\parallel$ dynamics and the three-field code with φ–$v_\parallel$–δp dynamics. Since there is transfer of energy between the fluctuations energies $E_{fl,1}$, $E_{fl,2}$ and $E_{fl,3}$ and

between the fluctuation and the background kinetic energies $\langle u_\perp^2 \rangle$ and $\langle u_\parallel^2 \rangle$ the conservation of the total energy requires many transfer terms to exactly balance. We find that the codes conserve the total energy well. In one test with all dissipation terms set zero and a large amplitude initial perturbation we find that over the time interval $tc_s/L_n = [0, 500]$, the total energy decreases by

$$E_T(0) - E_T(500) = 13.06273 - 13.06239 = 3.4 \times 10^{-4}$$

for a relative change of $(3.4/13) \times 10^{-4} \simeq 3 \times 10^{-5}$. In this test the background kinetic energy initially starts at zero, increases to approximately unity and settles down to fluctuate around 0.4. The variations in time of the three fluctuation energy components are order of unity.

In the first three cases of simulation, we study the parallel velocity shear driven mode with the self-consistent background flow evolution with and without the neoclassical damping effect from ν^{nc}. As shown in Ref. 9 with fixed background flow, the two field model equations (20) and (21) include linearly unstable modes driven by free energy released from parallel shear flow. However the background evolution with time is important because when the modes grow up, the fluctuation fields become large and the turbulent fluctuations significantly affect the profile of the background flow through the divergence of the Reynolds momentum transport tensors $\langle \tilde{v}_x \tilde{v}_\perp \rangle$ and $\langle \tilde{v}_x \tilde{v}_\parallel \rangle$ as shown in Eqs. (16) and (17). In the fourth case of the simulations, we study the shear flow generation in the ion temperature gradient driven or so-called $\eta_i (= d\ell nT_i/d\ell nn)$ mode case with the background neoclassical viscosity.

Case 1: Conversion of Toroidal Flow to Poloidal Flow Through Turbulence

In the first case 1A, we set $\nu^{nc} = 0$ and $\nu_\perp^a = \nu_\parallel^a = 0$, that is, there is no neoclassical flow, $S_0 = B_P/B_T = 0.2$ and the perpendicular viscosity $\mu_\perp = 0.01$ in the evolution of fluctuating fields only, $\mu_\perp = 0$ in the evolution of background flows. This case may be considered as the limit of a sufficiently high ion temperature plasma that the ion-ion collisional effects are negligible on the time scales of interest.

For the time interval t = 0–300(L_n/c_s), we keep the background flow fixed, that is, $u_\perp = u_\perp(x,t) = u_\perp(x,t=0) = 0$ and $u_\parallel = u_\parallel(x,t) = u_\parallel(x,t=0) = 6\sin(k_1 x)$ do not evolve in time throughout this time period [0, 300]. The modes are driven by $u_\parallel' = \partial u_\parallel/\partial x$. A saturated state of vortex turbulence is obtained at about $t = 160(L_n/c_s)$ to $t = 300(L_n/c_s)$ as shown in Figs. 2(a), 3(a), and 4(a) with rms fluctuation levels of $\tilde{u}_\perp = 0.3(v_{de})$ and $\tilde{u}_\parallel = 0.55(v_{de})$. At $t = 300(L_n/c_s)$ we turn on the background flow dynamical equations (16) and (17) (with $\nu^{nc} = \nu_\perp^a = \nu_\parallel^a = 0$), that is, we allow $u_\perp$ and $u_\parallel$ to evolve with time. The background poloidal energy ($E_{bg,1}$) is shown to immediately increase and the toroidal energy ($E_{bg,2}$) decrease in Figs. 2(b) and 3(b) to create a new stage with a mean helical shear flow. The turbulent fluctuations $\tilde{\varphi}$ and $\tilde{v}_\parallel$ are shown to be suppressed as the poloidal shear flow increases in Figs. 2 and 3 for $t > 300(L_n/c_s)$. Figure 4 is contour plots of φ at $t = 275(L_n/c_s)$ and $t = 395(L_n/c_s)$. Figure 4(b) shows that for $t > 300(L_n/c_s)$ the sheared poloidal flow generated is sufficient to produce mostly open stream lines which suppresses the turbulence and the turbulent transport shown in Fig. 4(b) where the poloidal flow is still zero. The turbulent momentum transport generates the poloidal shear flow while reducing the parallel shear flow as shown in Figs. 2, 3, and 4.

In the case 1B we set all the parameters and initial profiles to the same values as in case 1A, but let $u_\perp(x,t)$ and $u_\parallel(x,t)$ evolve with time from the beginning ($t = 0$). Like the case 1A, the modes are driven by $u_\parallel'$, however, the gradient drive now relaxes in time. A saturated

state is now obtained at around $t = 60(L_n/c_s)$ as shown in Fig. 5(a). After reaching this maximum at $t \simeq 60(L_n/c_s)$ the turbulence now immediately begins to decay in contrast to case 1A. Figures 5 and 6 are time evolutions of fluctuation (E_{fl}) and background (E_{bg}) energies for poloidal and toroidal flows, respectively. Figure 7 shows the time evolution of the mode fluctuations $\tilde{\varphi}(k_x, k_y = 1.0)$ for a spectrum of $k_x \rho_s \rightarrow k_x$ values. From Figs. 5 and 6, we can see that when $t < 40(L_n/c_s)$, the modes experience exponential growth at the growth rate $\gamma \lesssim 0.1 c_s/L_n$. When the turbulent fluctuations become large, as in the time interval $40 < tc_s/L_n < 80$, they drive up the poloidal flow in Fig. 5(b). While the shear of the poloidal flow is weak, it shows no effect of suppressing the growth of the fluctuations. However, when the poloidal shear flow gets strong, the mode fluctuations are effectively suppressed, and so the signals from the mode fluctuations become small for $t > 100(L_n/c_s)$ as shown in Fig. 7. We note from Fig. 6(b) that the toroidal flow energy decreases with time during the whole process. The most significant drop in the toroidal kinetic energy during the period $30 < tc_s/L_n < 80$ coincides with the rise of the poloidal kinetic energy during the peak of turbulent pulse. Part of the toroidal flow energy goes to poloidal flow and another part is damped through the viscous dissipation of the fluctuations. In the final state the ratio of the mean poloidal velocity ($u_\perp \sim 0.44(v_{de})$) to the mean toroidal velocity ($u_\parallel = 3.5(v_{de})$) is about 1/9.

Case 2: Neutral Beam Driven Toroidal Shear Flow

In this case we study the effect of nonambipolar flow on background flow. Physically the nonambipolar flow $u_\parallel^a$ can arise from neutral beam injection. We set $\nu_\parallel^a = 0.1$, $S_0 = 0.2$, $\mu_\perp = 0.01$ while keeping $\nu^{nc} = 0$, $\nu_\perp^a = 0$, and the externally driven variation in the toroidal profile $u_\parallel^a = 10 \sin(k_1 x)$. The spatially uniform $u_{0\parallel}$ part of $u_\parallel^a(x)$ is transformed away by going to the appropriate reference frame. From Eq. (15) this means that a nonuniform streaming parallel momentum with the finite value of the injection rate

$\nu_\parallel^a = 0.1$ and speed $u_\parallel^a$ now is injected into the plasma. The initial profiles for background flows are $u_\perp(x, t = 0) = 0$ and $u_\parallel(x, t = 0) = \sin(k_1 x)$, and the fluctuation fields are $\tilde{\varphi}(x, y, t = 0) = \tilde{v}_\parallel(x, y, t = 0) = 0.1 \exp\left(-\frac{x^2+y^2}{r_0^2}\right)$ with $r_0 = 6[\rho_s]$. In the beginning stage ($t = 0$–$100[L_n/c_s]$), $u_\parallel'$ is too weak to drive the modes unstable. However the toroidal shear flow increases during this time from the injected parallel flow $u_\parallel^a$, which gives a driving force for the toroidal shear flow $u_\parallel(x, t)$. When the neutral beam driven toroidal shear flow gets large, the shear flow drives the unstable modes. The fully developed fluctuation then transfer energy-momentum to the background poloidal flow through $\pi_{x\perp}$. The mean poloidal flow reaches about one half the mean toroidal flow velocity. With the increase of the poloidal shear flow, again the turbulent fluctuations of the modes are suppressed, but due to the continuous driving a well defined turbulent state is reached with $\tilde{u}_\perp \simeq 0.24(v_{de}) \gtrsim \tilde{u}_\parallel$. The whole process is shown in Figs. 8 and 9 giving the time evolution of the four energy components. A nonlinear regression fitting code is used here to determine the decay power of the turbulent fluctuation energy. The results show that the total fluctuation energy decays to a constant as $1/t^m$, with the decay index m in the range of 1.5 to 2.5 depending on the system parameter. For the kinetic energy in the parallel velocity fluctuations $E_{fl,2}(t)$ the parameterization is shown in Fig. 10. In Fig. 10, where the dashed line shows the fluctuation energy $E_{fl,2}$ versus time and solid line is the fitting curve that determines $m \simeq 2.3$ and the asymptotic value of $E_{fl,2}(\infty) \cong 0.008$ for this case.

Case 3: Effect of Neoclassical Flow and Damping on the Turbulence

In this case, we let $\nu^{nc} = 0.01$, $\nu_\perp^a = \nu_\parallel^a = 0$, $S_0 = 0.2$, $\mu_\perp = 0.01$ and the neoclassical flow profile $u^{nc} = 4\sin(k_1 x)$ and initially $u_\perp(x, t = 0) = 0$ and $u_\parallel(x, t = 0) = 20\sin(k_1 x)$. With these profiles, therefore the background flow is initially in the neoclassical equilibrium state so that $u_\perp - S_0 u_\parallel + u^{nc} = 0$. With evolution of time, the fluctuations first are driven up due to the parallel shear flow, then again when the background poloidal shear flow becomes

strong enough ($E_{bg,1} \sim 0.7$ or $u_\perp \sim 1(v_{de})$ in this case), the fluctuations are suppressed and decay as $1/t^m$ where $m \sim 1$ as shown in Figs. 11(a) and (b). Meanwhile the parallel shear flow becomes weak due to the release of its free energy to the fluctuations and the perpendicular shear flow as shown in Figs. 12(a) and (b). In the final turbulent state the mean flow fluctuation levels are $\widetilde{u}_\perp \simeq 1(v_{de})$ and $\widetilde{u}_\parallel \simeq 0.5(v_{de})$ similar to earlier cases.

Figure 13 shows the evolution of the mean square deviation of the helical flow field from the neoclassical equilibrium, which is monitored by

$$E_{nc}(t) = \left\langle (u_\perp - S_0 u_\parallel + u^{nc})^2 \right\rangle$$

with time. In the final state $\overline{E}_{nc} \lesssim 0.03$ showing that the background flow goes to another equilibrium state determined by the line $u_\perp^f - S_0 u_\parallel^f + u^{nc} \simeq 0$. The observed evolution is summarized in Fig. 14 where f means the final quasi-steady state. A quantitative example of the stability boundary for particular parameters is the $\gamma = 0$ limit of the contours in Fig. 1.

From other simulations not shown here we find that, in fact, we can start with any reasonable initial state for the background flow, that is, any point in parameter space in Fig. 14, and we find that the turbulent fluctuation will take the system along the equilibrium state line $u_\perp^f - S_0 u_\parallel^f + u^{nc} \simeq 0$ towards the linearly stable region shown in Fig. 14. This shows that the neoclassical damping ν^{nc} and the turbulent fluctuation always tend to stabilize the system. Therefore, in the systems studied the turbulent fluctuations can be maintained at a significant level only if there is either an exterior accelerating torque such as neutral beam injection as given in Case 2 to supply energy-momentum to drive the background parallel shear flow or an additional force such as the ion temperature gradient $(\partial T_i/\partial x)$, as studied in the next case, to directly drive the unstable modes. The driven fluctuations of the modes can then produce a continuous acceleration force on the background flow through the divergence of the Reynolds stress tensors.

Case 4: Shear flow generation and Ion Temperature Gradient Driven Fluctuations

In this case, we study shear flow generation in the η_i driven turbulence. We still use Eqs. (16) and (17) for the evolution of the background flows. For dynamical equations of the fields $\tilde{\varphi}$, $\tilde{v}_{\|}$ and $\tilde{p}$, we use Eqs. (1)–(3) in Ref. 22. The equations for $\tilde{\varphi}$ and $\tilde{v}_{\|}$ are similar to Eqs. (20) and (21) with a few changes: the toroidal curvature term $2\epsilon_n \partial\varphi/\partial y$ is added to the right-hand side of Eq. (20); the term $\nabla_{\|}\tilde{\varphi}$ at the right-hand side of Eq. (21) is changed to $\nabla_{\|}(\tilde{\varphi}+\tilde{p})$; and a third fluctuation equation or the thermal balance equation for the ion pressure $\tilde{p}$ is added. We set $\eta_i = 1.5$, toroidicity parameter $\epsilon_n = L_n/R = 0.1$, $\tau = T_e/T_i = 1$, $S_0 = 0.2$, $\Gamma = 5/3$, dimensionless viscosity $\mu_{\perp 1} = \mu_{\perp 2} = 0.2$ and dimensionless collisional thermal conductivity $\kappa = 0.1$ for the evolution of the fluctuation fields. We do not repeat the Hong-Horton equations here but refer the readers to Ref. 22.

In the 2D toroidal η_i-mode model the fluctuation levels in the absence of sheared flows gives large amplitude vortices that fill the simulation box. An example of the growth and saturation of the fluctuation energy without flow is shown in Fig. 15(a) which reproduces a case from Ref. 22.

For the case with shear flow generation, we set $\nu^{nc} = 0.0$, $u^{nc} = 0$, $\nu_{\perp}^{a} = \nu_{\|}^{a} = 0$. Initially, we set $u_{\perp}(x, t=0) = u_{\|}(x, t=0) = 0$. With evolution in time, the modes first are driven by ion temperature gradient, and background perpendicular and parallel flows then are driven through the divergences of the Reynolds stresses $\left\langle \tilde{v}_x \tilde{v}_{\|} \right\rangle$ and $\langle \tilde{v}_x \tilde{v}_{\perp} \rangle$. During the time period of $t = 0$–$180(L_n/c_s)$, which is the first nonlinear steady state, the linear growth stops at $t \sim 80(L_n/c_s)$ and from $t = 100 - 180(L_n/c_s)$ there is a well-defined steady state. The increase of the background shear flow significantly reduces the development of the fluctuation level as verified by comparing with the computer experiment without the background flow buildup in the same time period. Figure 15(a) shows that without the background shear flow, the total fluctuation energy is saturated as early as $t \sim 100(L_n/c_s)$

at $E_f \simeq 1400$. While with evolving background flow in Fig. 15(b), the total fluctuation energy growth stops first at $t \simeq 80(L_n/c_s)$ with $\overline{E}_f \simeq 35$ and the rms fluctuation level is about 6 times less than that in Fig. 15(a) in the first nonlinear state.

When the time progresses to $t \sim 600(L_n/c_s)$ in the system with the evolving shear flow, the saturation of the total fluctuation energy is observed as shown in Fig. 16(a). Figures 16(a) and 16(b) show that the saturation is characterized by the 180° out of phase oscillations of the fluctuation energy and background kinetic energy, which is caused by the energy exchanges between the fluctuations and the background through the energy fluxes given in Eq. (35). The total average fluctuation energy level, however, is about the same as that shown in Fig. 15(a) in which the background flow is fixed at $u_\perp = 0$ and $u_\parallel = 0$. This indicates that the background shear flow can greatly reduce the linear growth rate of the modes and the first nonlinear saturation level, but does not significantly affect the long-time limit saturation level of the average fluctuation in the nonlinear regime. Similar phenomena are also observed in earlier numerical studies for collisional drift wave turbulence and resistive pressure-gradient-driven turbulence by Carreras *et al.*[4,23]

The phenomena of nonlinear growth are further confirmed when we study the effects of the neoclassical damping. We made three numerical experiments with $\nu^{nc} = 0$, 0.01, and 0.1. The results show that although the neoclassical damping reduces the development and build-up of the background flow, especially reducing the perpendicular flow velocity, the time-average levels of the total fluctuation energies in the final stage in all three cases remain about the same as that in the case without the background flow shown in Fig. 15(a). For a clearer comparison, in Figs. 17(a) and (b) we plot the total fluctuation energies and background kinetic energies for the different ν^{nc} values, where the dot, solid and dashed line are for $\nu^{nc} = 0.1$, 0.01 and 0, respectively. As we can see from Figs. 17(a) and (b), at the final saturation stage although the background kinetic energy levels are quite different for the different ν^{nc}, the fluctuation energy levels have no significant difference. The results for

the variation of ν^{nc} are summarized in Table I.

All the numerical experiments in Table I are done with the same small scale viscosity in order to demonstrate the interaction between the turbulence and the flow. If the large scale viscosity is applied in the system, the turbulence will be significantly suppressed and fluctuation levels will be much lower, and therefore the flow energy level will be much lower also, since the background flow is driven by the turbulence.

In these numerical experiments we have found that the nonlinear growth is characterized by the series of turbulent pulses shown in Fig. 16(a) and the pulses cause intermittent transport state as shown in Figs. 15(b) and 16. Further studies and analysis on the phenomena and their effect on the system are needed and will be given elsewhere. In associated work by Tajima and Horton[25] intermittent transport for the η_i turbulence coupled to the background shear flow has also been found from low degree of freedom model of the driven system. In a future work the low degree of freedom model of Tajima and Horton will be compared with the nonlinear pde behavior reported here.

V Summary and Conclusions

In this work, we have studied the neoclassical viscosity control of shear flow generation through the interaction of drift wave turbulence with the self-consistent background flow profile evolution. Both parallel velocity shear driven turbulence and ion temperature gradient driven turbulence are presented. In the simulations the perpendicular and parallel background mean flows self-consistently evolve with time and are modified by the plasma turbulence through the Reynolds stress. The generation of the background shear flow therefore is a result of the coupling between the turbulent fluctuations and the background mean flow. In a nonuniform toroidal magnetic field, the neoclassical viscosity effect acts as a drag force which transfers the kinetic energy in the poloidal rotation into thermal energy.

We show when the fluctuation is driven by the free energy released from the parallel

velocity shear, without external energy supply (such as neutral beam injection), the toroidal plasma always relaxes from an unstable state to a stable state along an equilibrium path which is determined by the neoclassical condition $u_\perp - S_0 u_\parallel + u^{nc} = 0$ from Eqs. (16) and (17). Typically the development of the $u'_\parallel$ driven turbulence is the following: parallel shear flow drives the fluctuations by releasing the free energy stored in the sheared toroidal velocity profile. The fully developed fluctuations then push on the background and drive the perpendicular shear flow through the divergence of the Reynolds stress $\langle \tilde{v}_x \tilde{v}_\perp \rangle$. Thus if the neoclassical transport coefficient ν^{nc} is small, the perpendicular shear flow will grow large and then suppresses the turbulence. If ν^{nc} is large, however, the background flow will rapidly relax to an equilibrium state given by $u_\perp - S_0 u_\parallel + u^{nc} = 0$ (where $S_0 = B_p/B_T$). Therefore the magnitude of $u_\perp$ depends on the neoclassical flow $u^{nc}(x)$ given in Eq. (11). In the case where du^{nc}/dx is large, the perpendicular shear can rather abruptly become strong enough to suppress the turbulence. A similar abrupt stabilization of the turbulence is also observed by Sugama and Horton[7] using resistive-g turbulence. In both cases (large or small ν^{nc}), the poloidal flow loses energy to the plasma due to the neoclassical viscosity force defined in Eq. (11), which is also called the magnetic pumping effect. Therefore the system finally goes to a stable state with the turbulence being the mechanism for the evolution.

For an open system in which an external source keeps supplying energy to the system, as in the cases of the neutral beam injection and the ion temperature gradient driven mode, the saturation can be achieved when the external driving forces are balanced by the large-scale neoclassical viscosity damping and the small-scale viscous and thermal dissipation. The results of two dimensional simulations have shown that the generation of the perpendicular shear flow can effectively reduce the growth rate and slow down the development of the fluctuations. Additional considerations for the shear flow control of turbulent transport including the effect of poloidal asymmetry in the anomalous flux and the role of biased probes is given by Hassam *et al.*[24]

In the case of a strong ion temperature gradient driven toroidal mode, without magnetic shear, we find that the nonlinear evolution of the poloidal velocity profile keeps allowing a sequence of modes to go unstable that in turn allows an overall nonlinear growth of the spectrum up to the level found in the absence of the poloidal shear flow. Thus, it appears that in the late nonlinear stage, the background shear flow has no significant effect on the saturation level of turbulent fluctuations. In other words, the background shear flow can greatly delay the occurrence of the high level of turbulent fluctuations and the associated transport, but it does not finally eliminate the turbulent transport as previously thought. The nature of the time dependence of the transport is predicted to change from a steady state transport to an intermittent transport state. In the simulation the bursts occur on the time scale of $100(L_n/c_s) \sim 100\mu$ sec. Further study is required to obtain the parametric dependence of the intermittency and the associated effective transport rates.

Acknowledgments

The authors acknowledge useful discussions with H.V. Wong and F.L. Waelbroeck. The work was supported by the U.S. Department of Energy contract #DE-FG05-80ET-53088.

References

1. K.C. Shaing and E.C. Crume, Jr., Phys. Rev. Lett. **63**, 2369 (1989).

2. J.F. Drake, J.M. Finn, P. Guzdar, V. Shapiro, V. Shevchenko, F. Waelbroeck, A.B. Hassam, C.S. Liu, and R. Sagdeev, Phys. Fluids B **4**, 488 (1992).

3. P.H. Diamond and Y.B. Kim, Phys. Fluids B **3**, 1626 (1991).

4. B.A. Carreras, V.E. Lynch, L. Garcia, and P.H. Diamond, Phys. Fluids B **5**, 1491 (1993).

5. K.C. Shaing, Phys. Fluids B **4**, 171 (1992).

6. S. Hamaguchi and W. Horton, Phys. Fluids B **4**, 319 (1992).

7. H. Sugama and W. Horton, Shear Flow Generation by Reynolds Stress and Suppression of Resistive g Modes, Phys. Plasmas **1**, 345 (1994).

8. J.Q. Dong and W. Horton, Phys. Fluids B **5**, 1581 (1993).

9. W. Horton, J.Q. Dong, X.N. Su and T. Tajima, J. Geophys. Res. **98**, 13377 (1993).

10. M. Artun and W.M. Tang, Phys. Fluids B **4**, 1102 (1992).

11. F.L. Waelbroeck, T.M. Antonsen, Jr., P.N. Guzdar and A.B. Hassam, Phys. Fluids B **4**, 2441 (1992).

12. S.P. Hirshman, Phys. Fluids **21**, 224 (1978).

13. A.B. Hassam and R.M. Kulsrud, Phys. Fluids **21**, 2271 (1978).

14. S.P. Hirshman, Nucl. Fusion **18**, 917 (1978).

15. A.A. Ware and J.C. Wiley, Phys. Fluids **24**, 936 (1981).

16. S.P. Hirshman and D.J. Sigmar, Phys. Fluids **20**, 418 (1977).

17. R.D. Hazeltine, Phys. Fluids **17**, 961 (1974).

18. X.N. Su, W. Horton, and P.J. Morrison, Phys. Fluids B 4, 1238 (1992).

19. X.N. Su, Drift wave coherent vortex structures in inhomogeneous plasmas, Dissertation, The Univ. of Texas at Austin, (1992).

20. A.D. Beklemishev and W. Horton, Phys. Fluids B **4**, 200 and 2176 (1992).

21. H. Sugama, A.D. Beklemishev, and W. Horton, *Comments on Single-helicity versus multi-helicity simulations,* Proceedings of U.S.-Japan Workshop on η_i mode, Austin, Texas, January, 1993.

22. B.G. Hong and W. Horton, Phys. Fluids B **2**, 978 (1990).

23. B.A. Carreras, K. Sidikman, P.H. Diamond, P.W. Terry, and L. Garcia, Phys. Fluids B 4, 3115 (1992).

24. A.B. Hassam, T.M. Antonsen, Jr., J.F. Drake, P.N. Guzdar, C.S. Liu, D.R. McCarthy, and F.L. Waelbroeck, Phys. Fluids B **5**, 2519 (1993).

25. T. Tajima, Y. Kishimoto, M.J. LeBrun, M.G. Gray, J.Y. Kim, W. Horton, H. Vernon Wong, and M. Kotschenreuther, "Transport in the Self-Organized Relaxed State of Ion Temperature Gradient Instability," in *Ion Temperature Gradient-Driven Turbulent Transport*, Eds. W. Horton, A. Wootton, and M. Wakatani, (AIP Conference Proceedings, January, 1994), p. 255.

Figure Captions

1. (a) Normalized growth rate contour in the $(u'_{\parallel}, u'_{\perp})$ plane for magnetic shearless configuration with $k_y\rho_s = 1$ and $S_0 = B_p/B_T = 0.2$. (b) Normalized growth rate contour in the $(u'_{\parallel}, u'_{\perp})$ plane for slab geometry with magnetic shear, $k_y\rho_s = 1$ and $s = L_n/L_s = 0.1$ where $B_p/B_T = x/L_s$.

2. Time evolutions of (a) the turbulent fluctuation energy $E_{fl,1}$ and (b) perpendicular background flow energy $E_{bg,1}$ in case 1A. For $t < 300(L_n/c_s)$, the perpendicular background flow $u_{\perp} = 0$ fixed. When $t > 300(L_n/c_s)$, $u_{\perp}$ evolves with time according to Eq. (16) with $\nu^{nc} = 0$ and $\nu^a_{\perp} = \nu^a_{\parallel} = 0$.

3. Time evolutions of (a) the turbulent fluctuation energy $E_{fl,2}$ and (b) parallel background flow energy $E_{bg,2}$ in case 1A. For $t < 300(L_n/c_s)$, the parallel background flow $u_{\parallel} = 6\sin(k_1 x)(\rho_s c_s/L_n)$ fixed. When $t > 300(L_n/c_s)$, $u_{\parallel}$ evolves with time according to Eq. (17) with $\nu^{nc} = 0$ and $\nu^a_{\perp} = \nu^a_{\parallel} = 0$.

4. The contour plot of $\varphi(x, y, t)$ in case 1A. (a) At $t = 275(L_n/c_s)$ and (b) at $t = 395(L_n/c_s)$.

5. Time evolutions of (a) the turbulent fluctuation energy $E_{fl,1}$ and (b) perpendicular background flow energy $E_{bg,1}$ in case 1B.

6. Time evolutions of (a) the turbulent fluctuation energy $E_{fl,2}$ and (b) parallel background flow energy $E_{bg,2}$ in case 1B.

7. Time evolutions of individual mode fluctuation of $\tilde{\varphi}(k_x, k_y = 1.0)$ for a spectrum of $k_x\,\rho_s$ values.

8. Time evolutions of (a) the turbulent fluctuation energy $E_{fl,1}$ and (b) perpendicular background flow energy $E_{bg,1}$ when a counter parallel stream of beam with speed $u_{\|}^{a} = 10\sin(k_1 x)(\rho_s c_s/L_n)$ is being injected into the plasma in case 2.

9. Time evolutions of (a) the turbulent fluctuation energy $E_{fl,2}$ and (b) parallel background flow energy $E_{bg,2}$ when a counter parallel stream of beam with speed $u_{\|}^{a} = 10\sin(k_1 x)(\rho_s c_s/L_n)$ is being injected into the plasma in case 2.

10. Time evolution of the total fluctuation energy $E_{fl,2}(t)$ in case 2. The dashed line shows the E_{fl} versus time t and the solid line is the fitting curve obtained from the nonlinear regression fit to the parameterization $E_{fl,2}(\infty) + \Delta E/t^m$.

11. Time evolutions of (a) the turbulent fluctuation energy $E_{fl,1}$ and (b) perpendicular background flow energy $E_{bg,1}$ with neoclassical coefficient $\nu^{nc} = 0.01$ in case 3.

12. Time evolutions of (a) the turbulent fluctuation energy $E_{fl,2}$ and (b) parallel background flow energy $E_{bg,2}$ with neoclassical coefficient $\nu^{nc} = 0.01$ in case 3.

13. Time evolution of the quantity $E_{nc} = \left\langle (u_\perp - S_0 u_{\|} + u^{nc})^2 \right\rangle$ in case 3.

14. Qualitative description of the background flow state evolution. The curve represents the marginal instability of the parallel shear flow driven mode and the straight line represents the equilibrium path line $u_\perp - S_0 u_{\|} + u^{nc} = 0$ in case 3.

15. Time evolutions of the total fluctuation energy of (a) fixed background ($u_\perp$ and $u_{\|} = 0$) and (b) evolving background (with $\nu^{nc} = 0$) in η_i mode case in the time interval $t = 0$–$200(L_n/c_s)$.(case 4).

16. Time evolutions of (a) the total fluctuation energy and (b) the background flow energy (with $\nu^{nc} = 0$) in the time interval $t = 0$–$1000(L_n/c_s)$. The saturation is observed at

around $t \sim 600(L_n/c_s)$. During the saturation the oscillations of the background and fluctuation energies look like mirror image of each other.

17. Time evolutions of (a) the total fluctuation energies and (b) the total background energies for different neoclassical coefficients. Dot, solid and dashed lines are for ν^{nc}=0.1, 0.01 and 0, respectively.

ν^{nc}	$\sqrt{2E_{f\ell,l}}$	$\sqrt{2E_{bg,1}}$
0	50	50
0.01	47	17
0.1	45	7
1.0	45	2.5

Table I: Variation of Final Fluctuation and Background Energies with the Neoclassical Damping

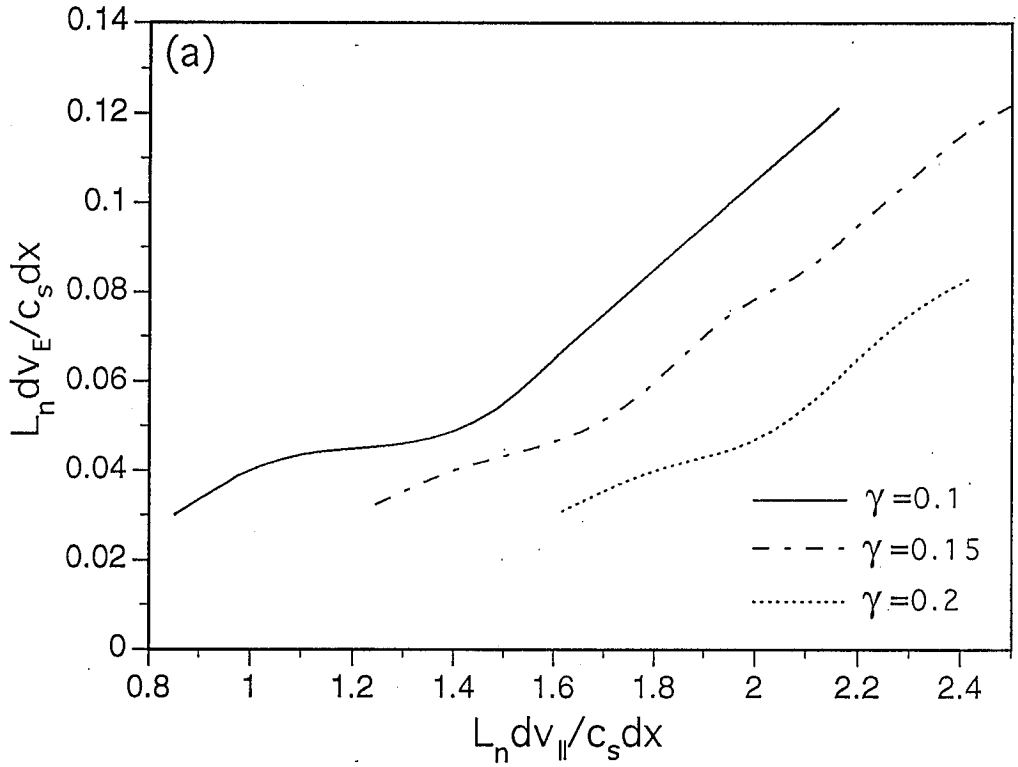
(a)
0.14
0.12
0.1
0.08
0.06
0.04
0.02
0
0.8
1
1.2
1.4
1.6
1.8
2
2.2
2.4
$L_n dv_E/c_s dx$
$L_n dv_{||}/c_s dx$
γ =0.1
γ =0.15
γ =0.2

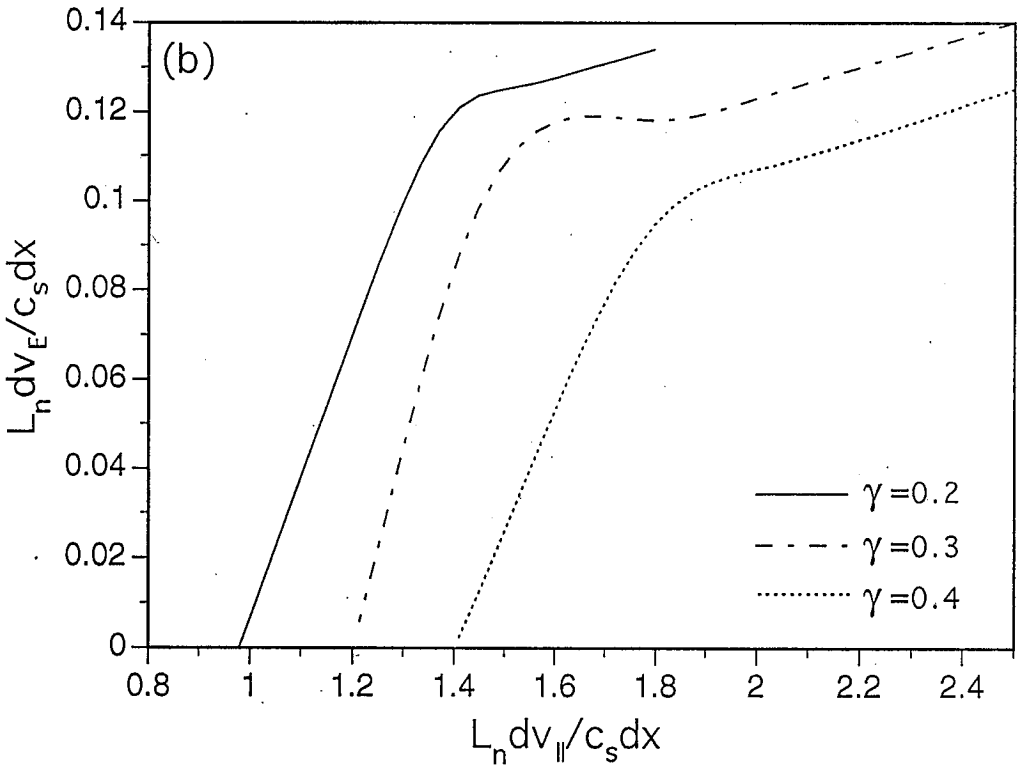
(b)
0.14
0.12
0.1
0.08
0.06
0.04
0.02
0
0.8
1
1.2
1.4
1.6
1.8
2
2.2
2.4
$L_n dv_E/c_s dx$
$L_n dv_{||}/c_s dx$
γ =0.2
γ =0.3
γ =0.4

Figure 1

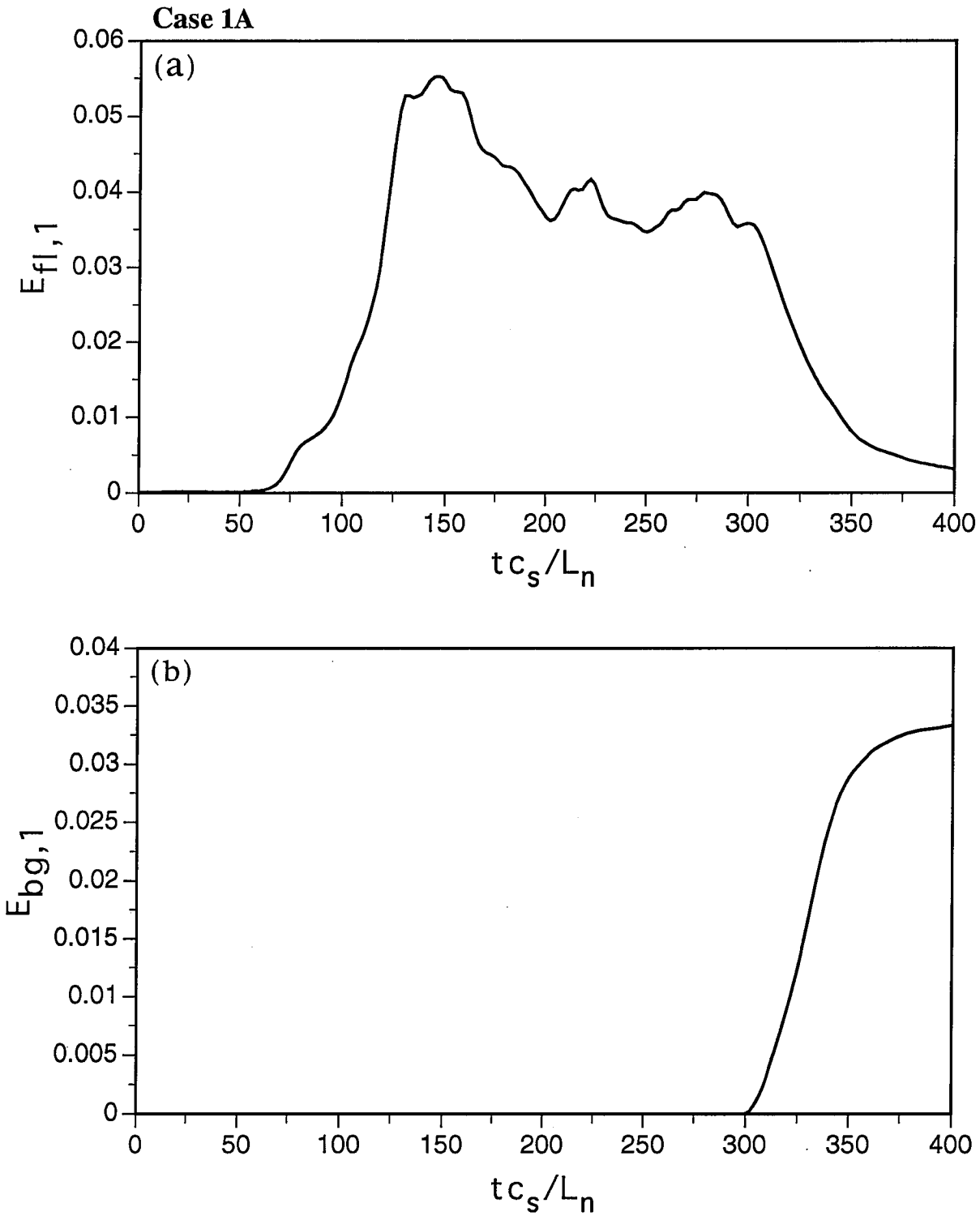
Case 1A
(a)
0.06
0.05
0.04
0.03
0.02
0.01
0
$E_{fl,1}$
0
50
100
150
200
250
300
350
400
tc_s/L_n
(b)
0.04
0.035
0.03
0.025
0.02
0.015
0.01
0.005
0
$E_{bg,1}$
0
50
100
150
200
250
300
350
400
tc_s/L_n

Figure 2

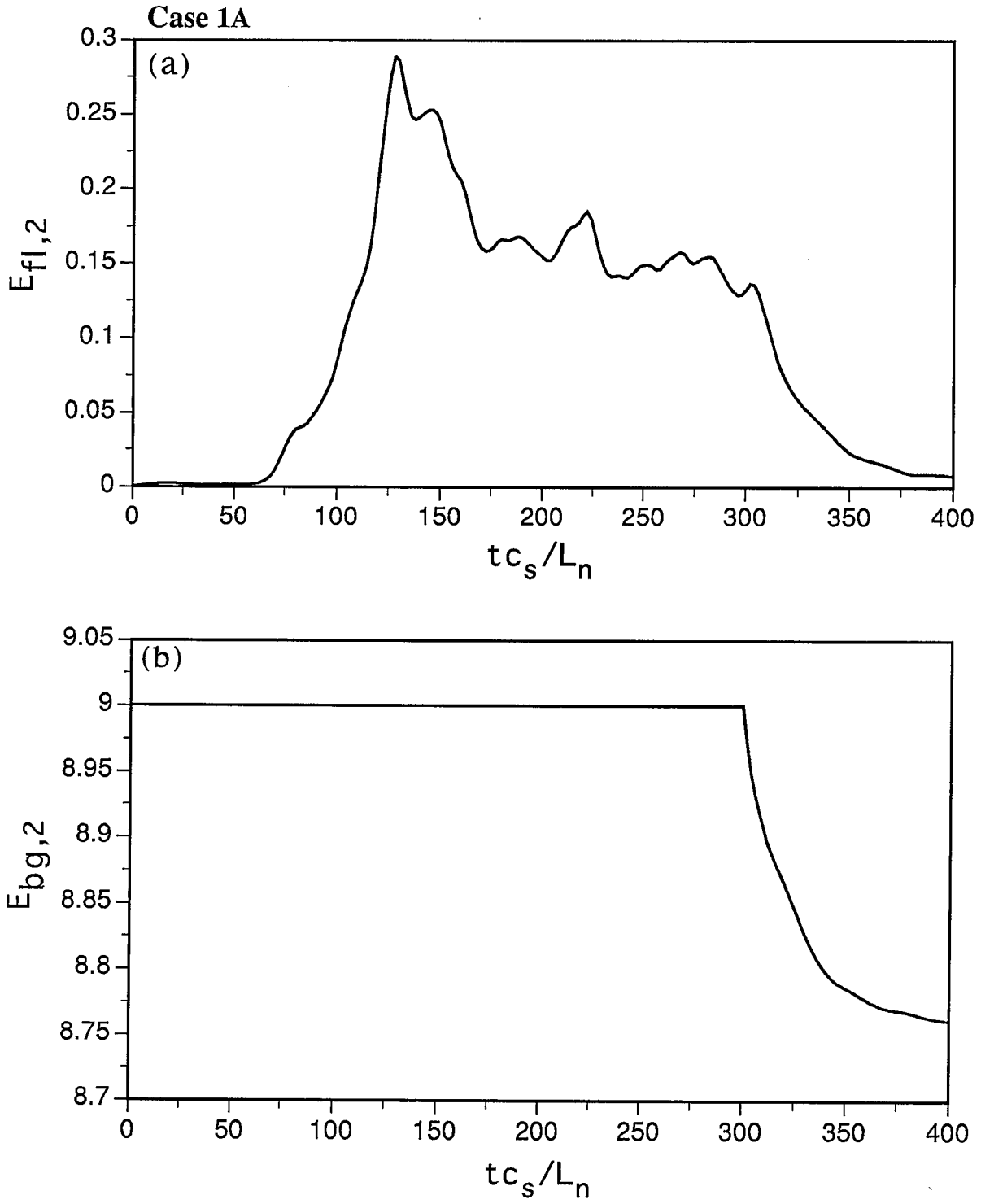
Case 1A
(a)
0.3
0.25
0.2
0.15
0.1
0.05
0
$E_{fl,2}$
0
50
100
150
200
250
300
350
400
tc_s/L_n
(b)
9.05
9
8.95
8.9
8.85
8.8
8.75
8.7
$E_{bg,2}$
0
50
100
150
200
250
300
350
400
tc_s/L_n

Figure 3

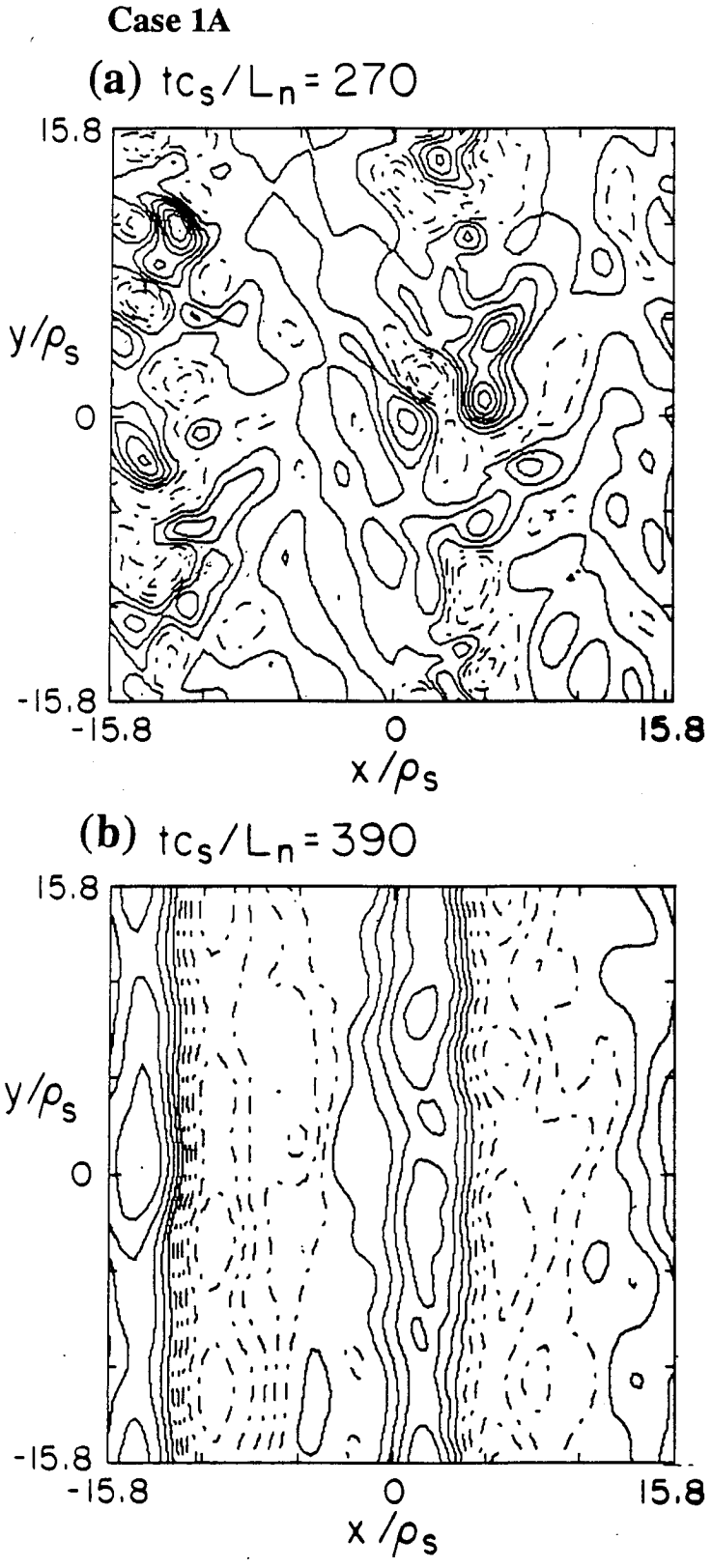
Case 1A
(a) $tc_s/L_n = 270$
15.8
y/ρ_s
0
-15.8
-15.8
0
15.8
x/ρ_s
(b) $tc_s/L_n = 390$
15.8
y/ρ_s
0
-15.8
-15.8
0
15.8
x/ρ_s

Figure 4

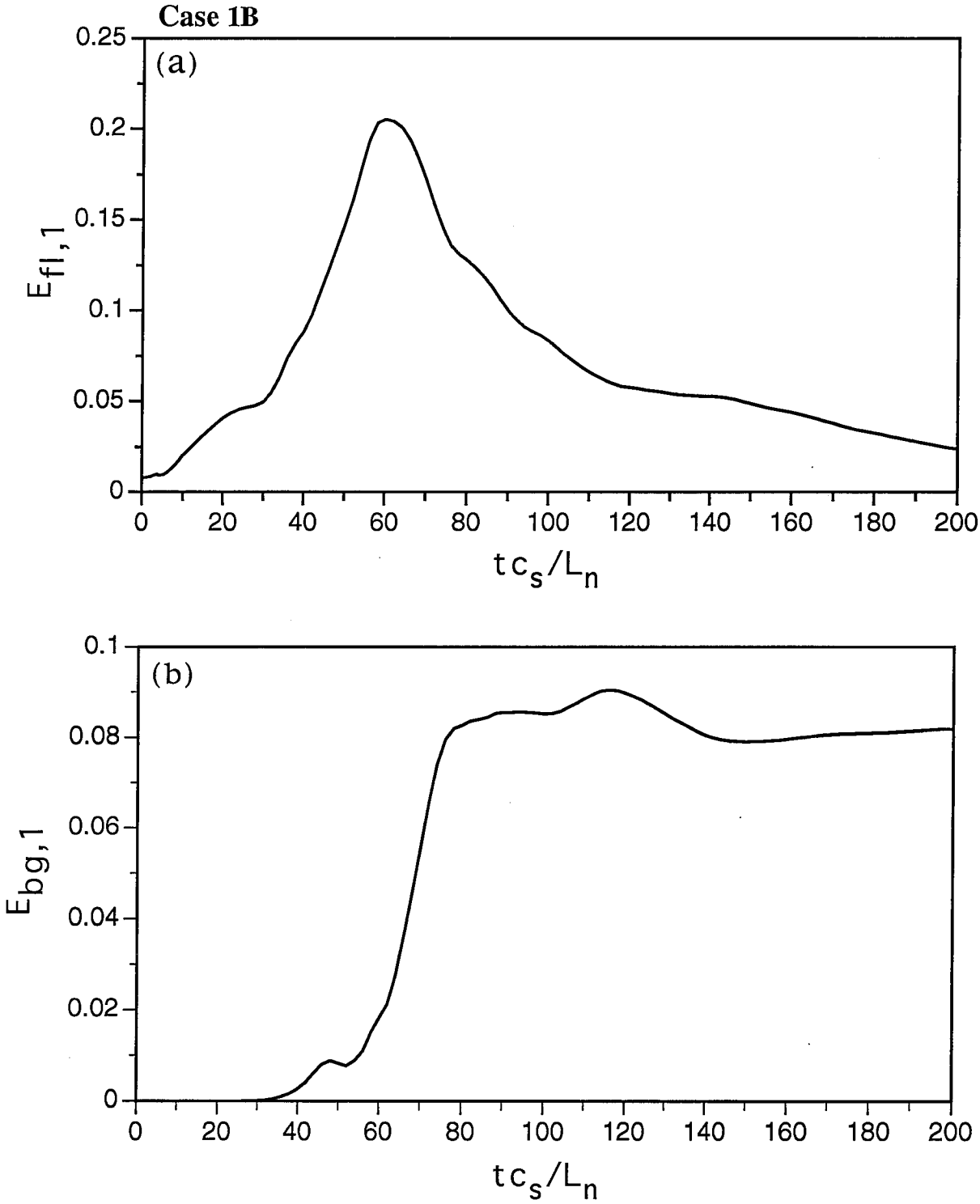
Case 1B
(a)
0.25
0.2
0.15
0.1
0.05
0
$E_{fl,1}$
0
20
40
60
80
100
120
140
160
180
200
tc_s/L_n
(b)
0.1
0.08
0.06
0.04
0.02
0
$E_{bg,1}$
0
20
40
60
80
100
120
140
160
180
200
tc_s/L_n

Figure 5

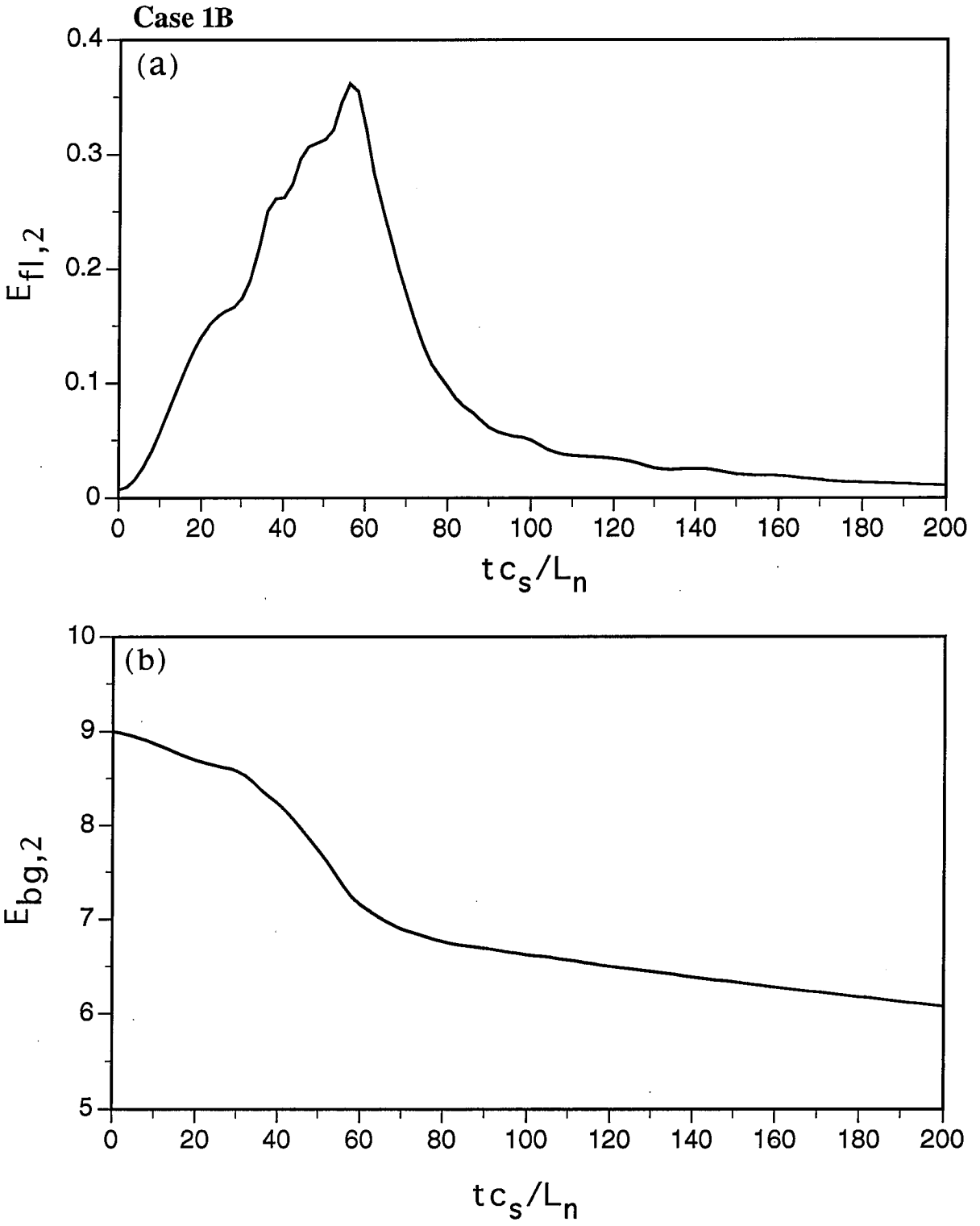
Case 1B
(a)
0.4
0.3
0.2
0.1
0
$E_{fl,2}$
0
20
40
60
80
100
120
140
160
180
200
tc_s/L_n
(b)
10
9
8
7
6
5
$E_{bg,2}$
0
20
40
60
80
100
120
140
160
180
200
tc_s/L_n

Figure 6

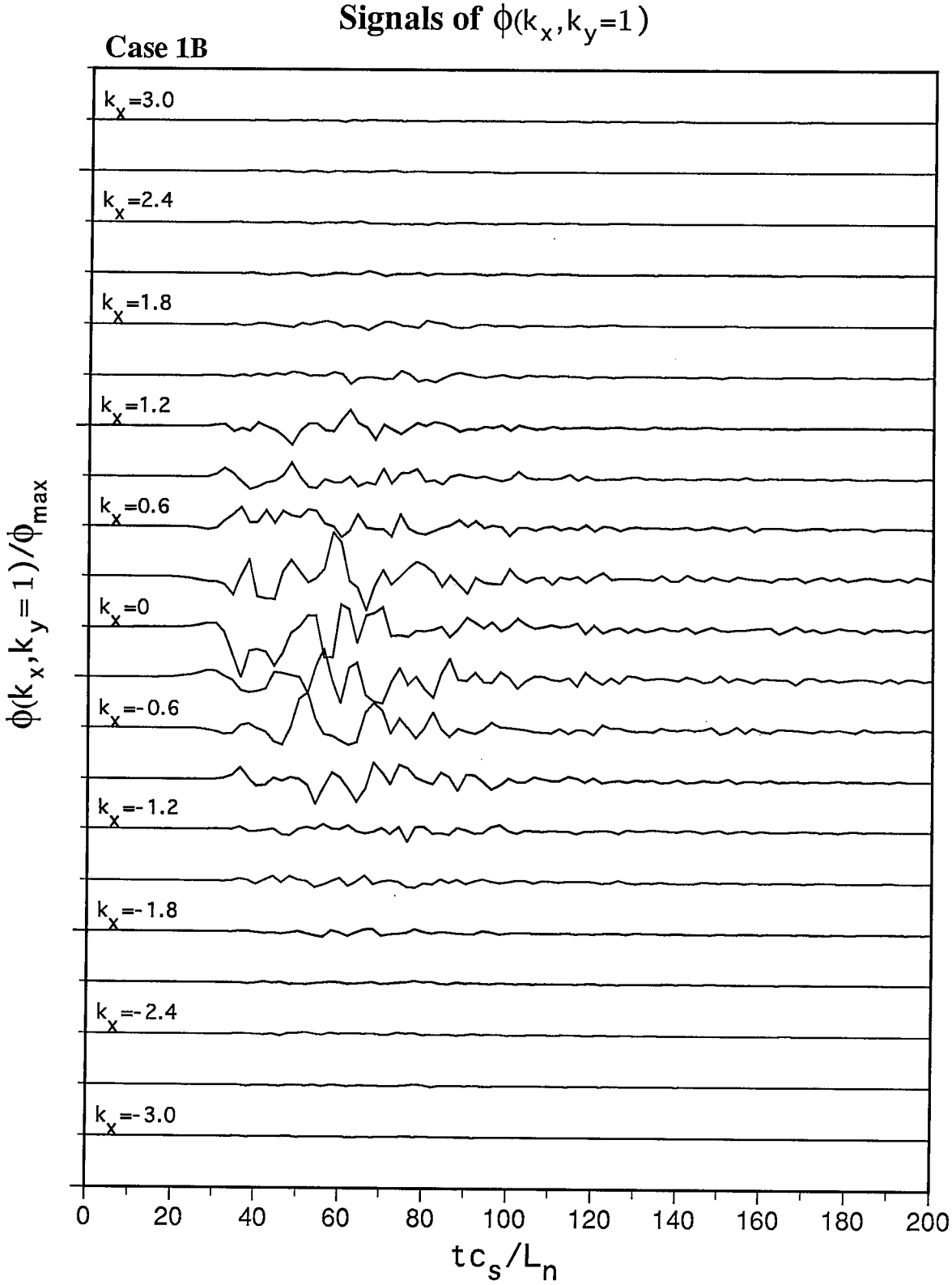
Signals of $\phi(k_x, k_y=1)$
Case 1B
k_x=3.0
k_x=2.4
k_x=1.8
k_x=1.2
k_x=0.6
k_x=0
k_x=-0.6
k_x=-1.2
k_x=-1.8
k_x=-2.4
k_x=-3.0
$\phi(k_x, k_y=1)/\phi_{max}$
0
20
40
60
80
100
120
140
160
180
200
tc_s/L_n

Figure 7

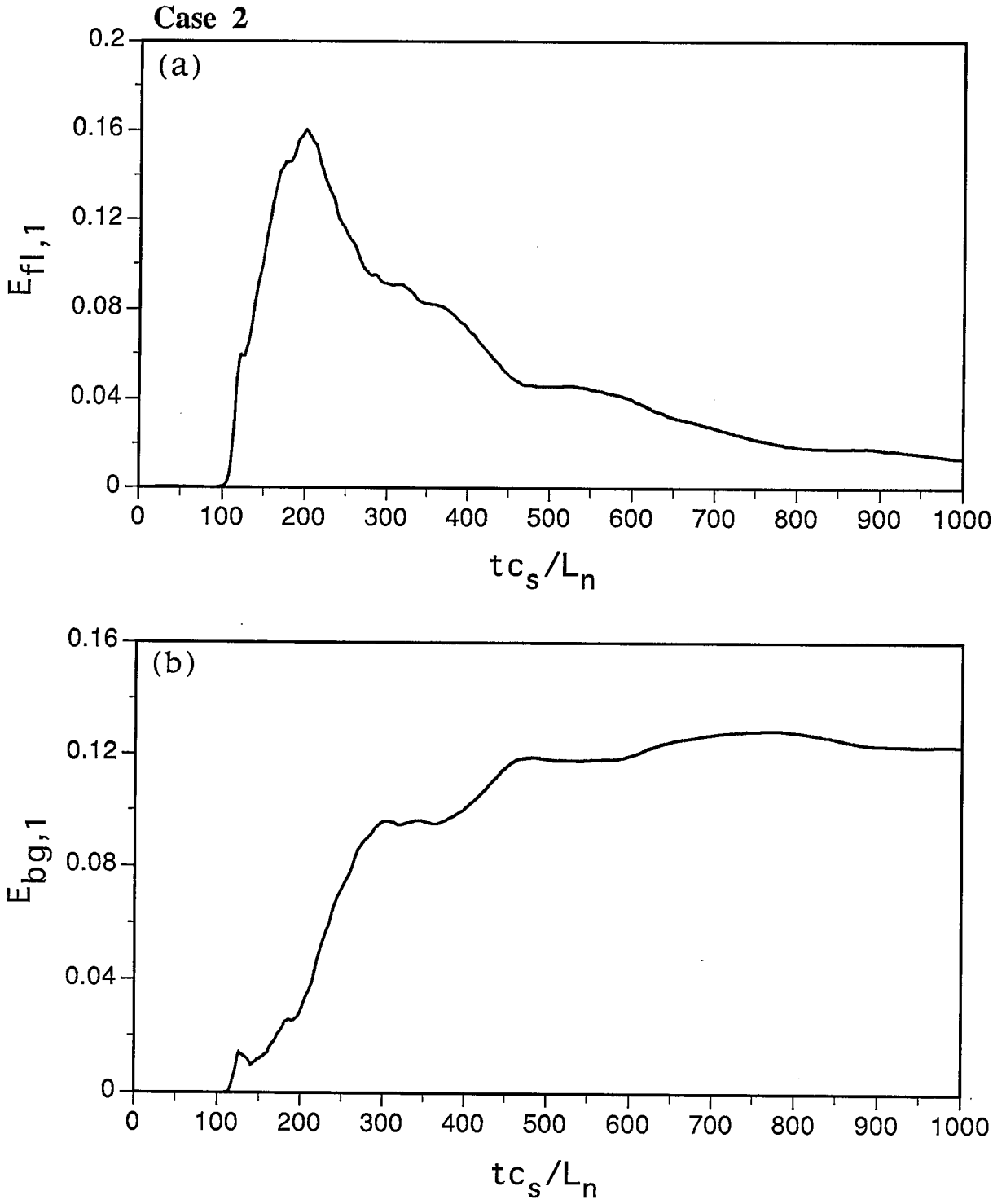
Case 2
(a)
0.2
0.16
0.12
0.08
0.04
0
$E_{fl,1}$
0
100
200
300
400
500
600
700
800
900
1000
tc_s/L_n
(b)
0.16
0.12
0.08
0.04
0
$E_{bg,1}$
0
100
200
300
400
500
600
700
800
900
1000
tc_s/L_n

Figure 8

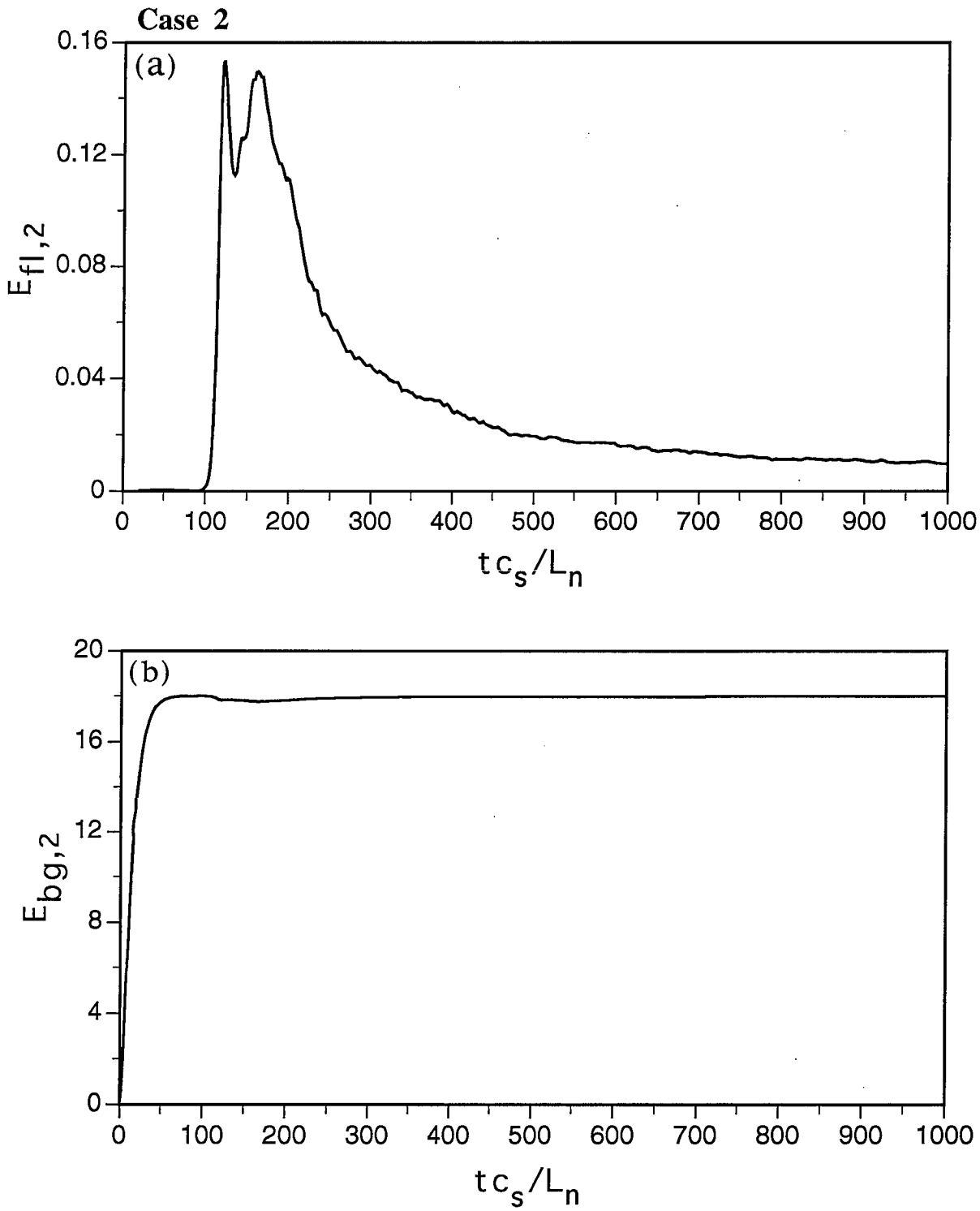
Case 2
(a)
0.16
0.12
0.08
0.04
0
$E_{fl,2}$
0
100
200
300
400
500
600
700
800
900
1000
tc_s/L_n
(b)
20
16
12
8
4
0
$E_{bg,2}$
0
100
200
300
400
500
600
700
800
900
1000
tc_s/L_n

Figure 9

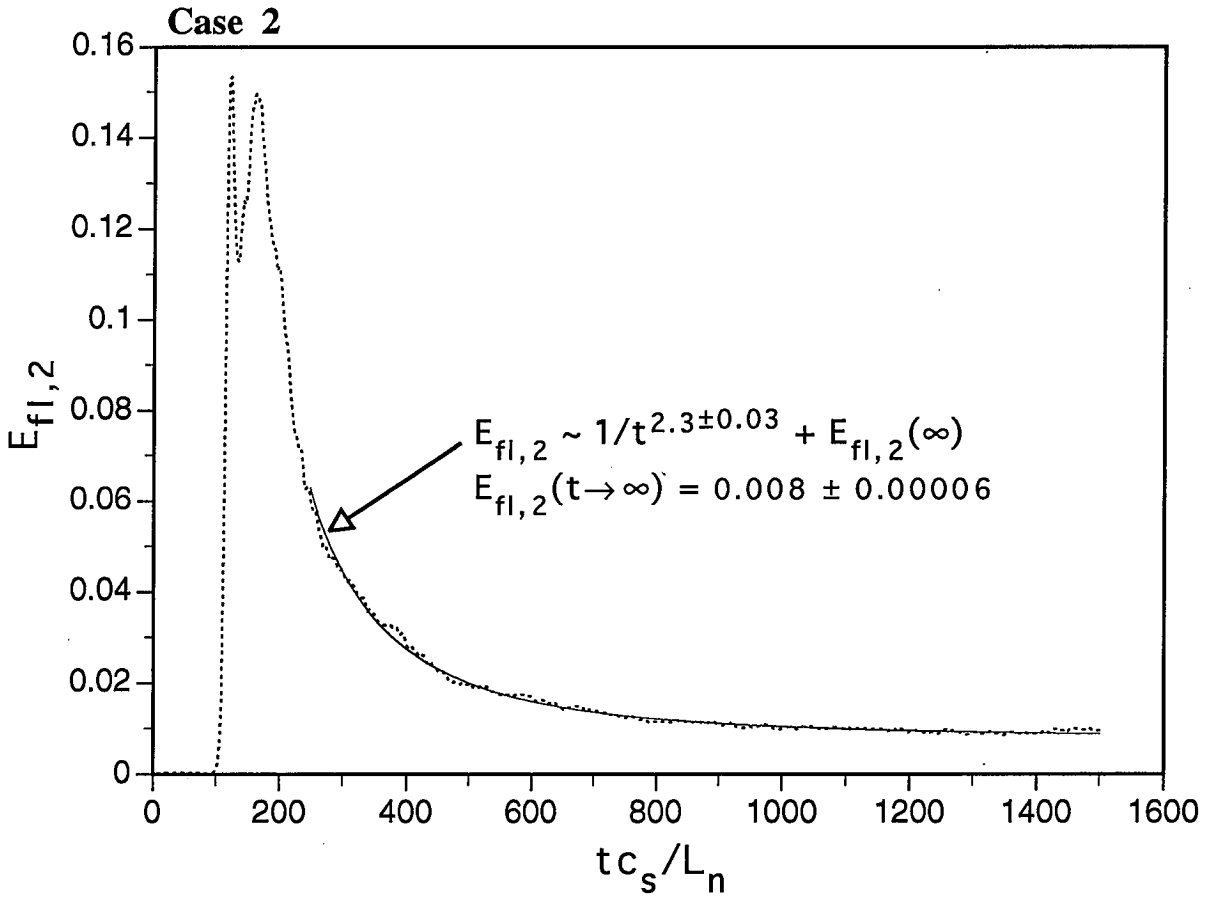
Case 2
0.16
0.14
0.12
0.1
0.08
0.06
0.04
0.02
0
$E_{fl,2}$
$E_{fl,2} \sim 1/t^{2.3\pm0.03} + E_{fl,2}(\infty)$
$E_{fl,2}(t\rightarrow\infty) = 0.008 \pm 0.00006$
0
200
400
600
800
1000
1200
1400
1600
tc_s/L_n

Figure 10

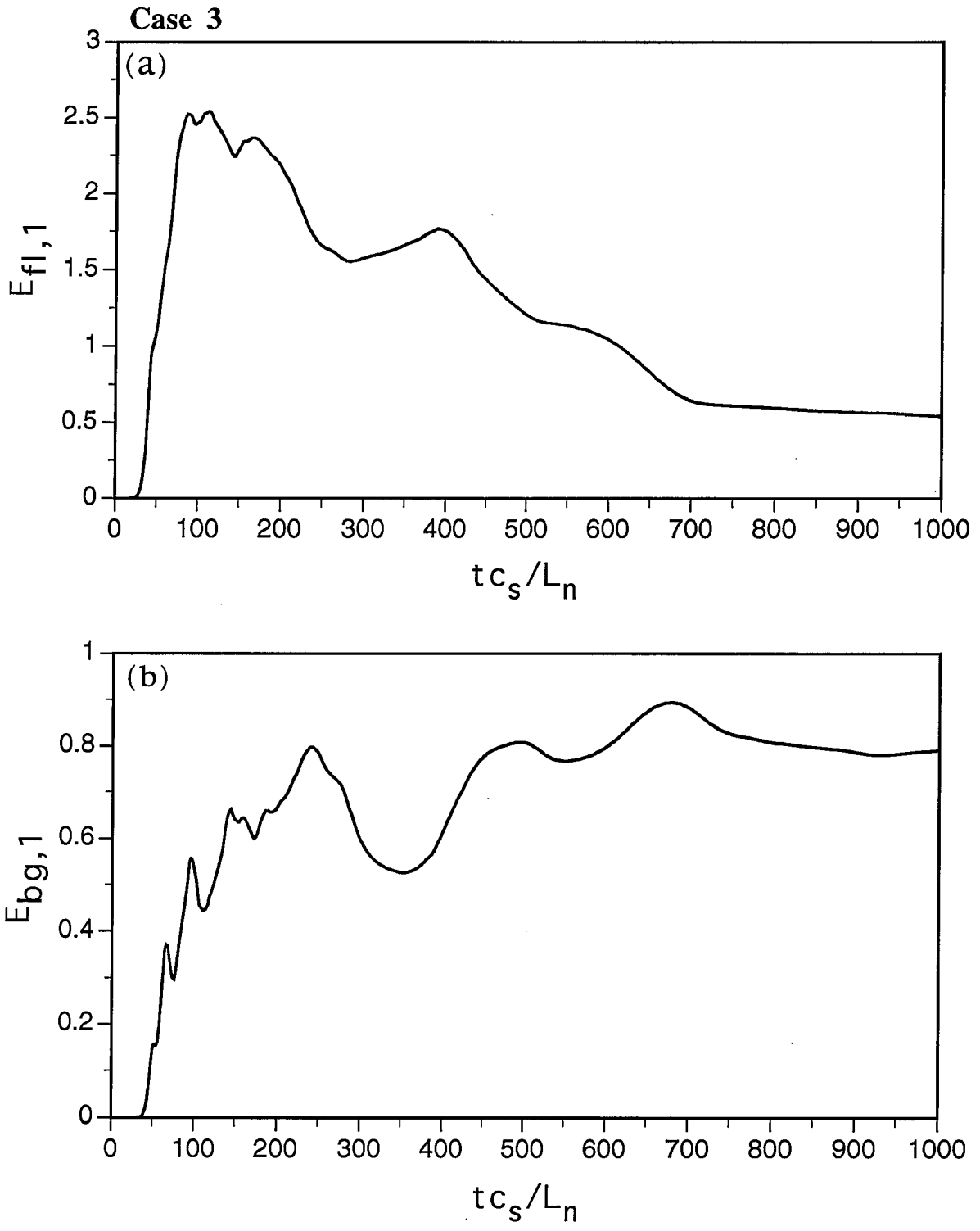

Figure 11

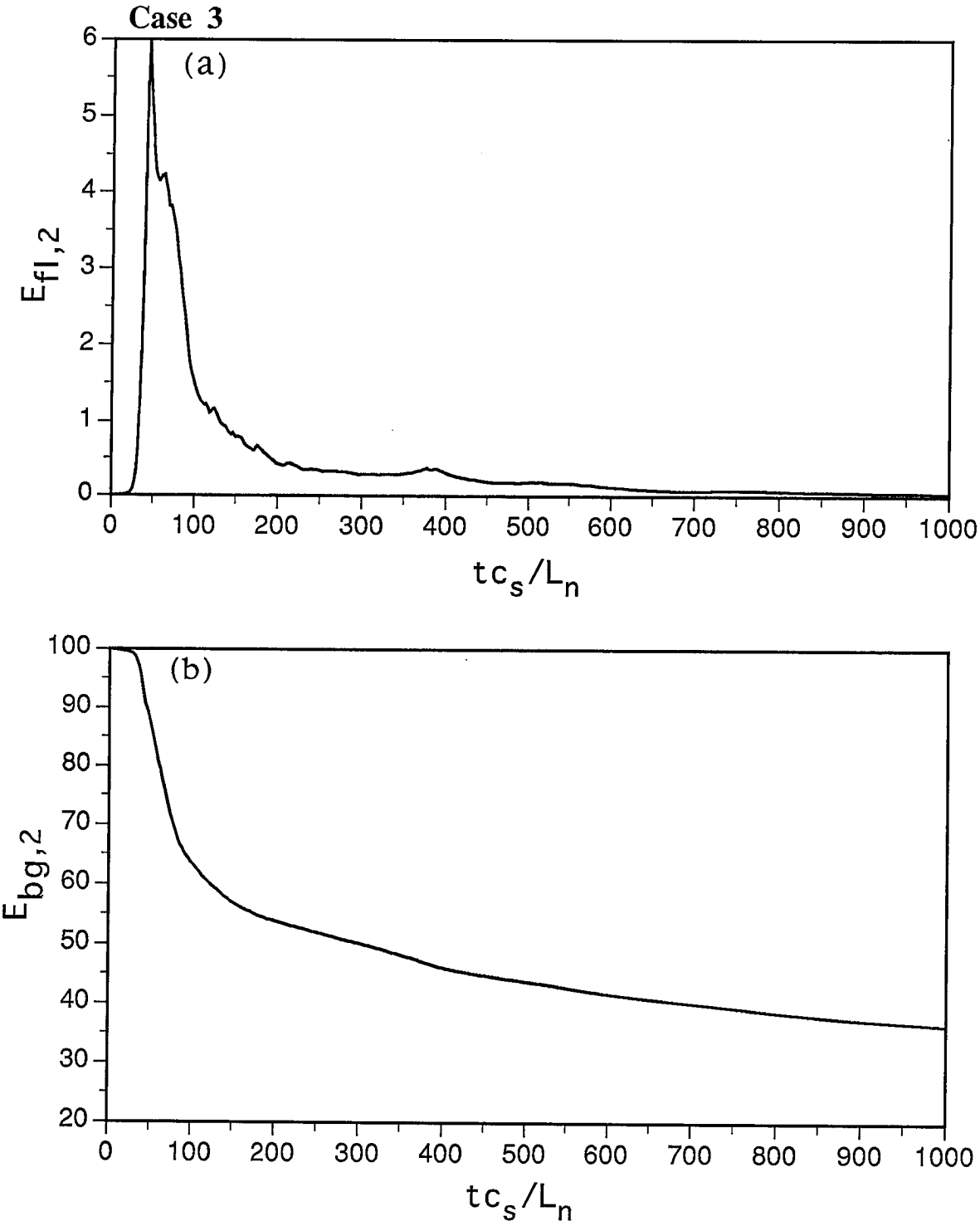

Figure 12

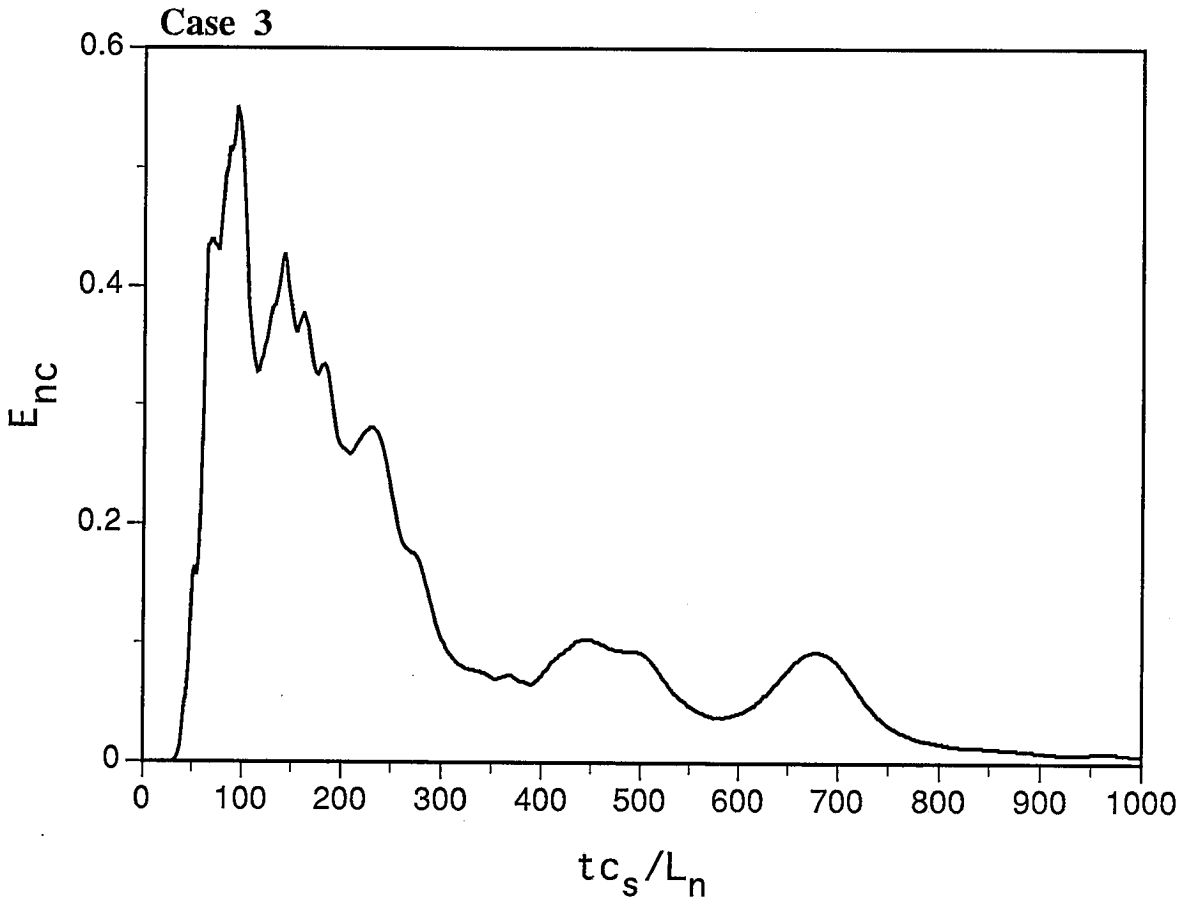
Case 3
0.6
0.4
0.2
0
E_{nc}
0
100
200
300
400
500
600
700
800
900
1000
tc_s/L_n

Figure 13

Case 3

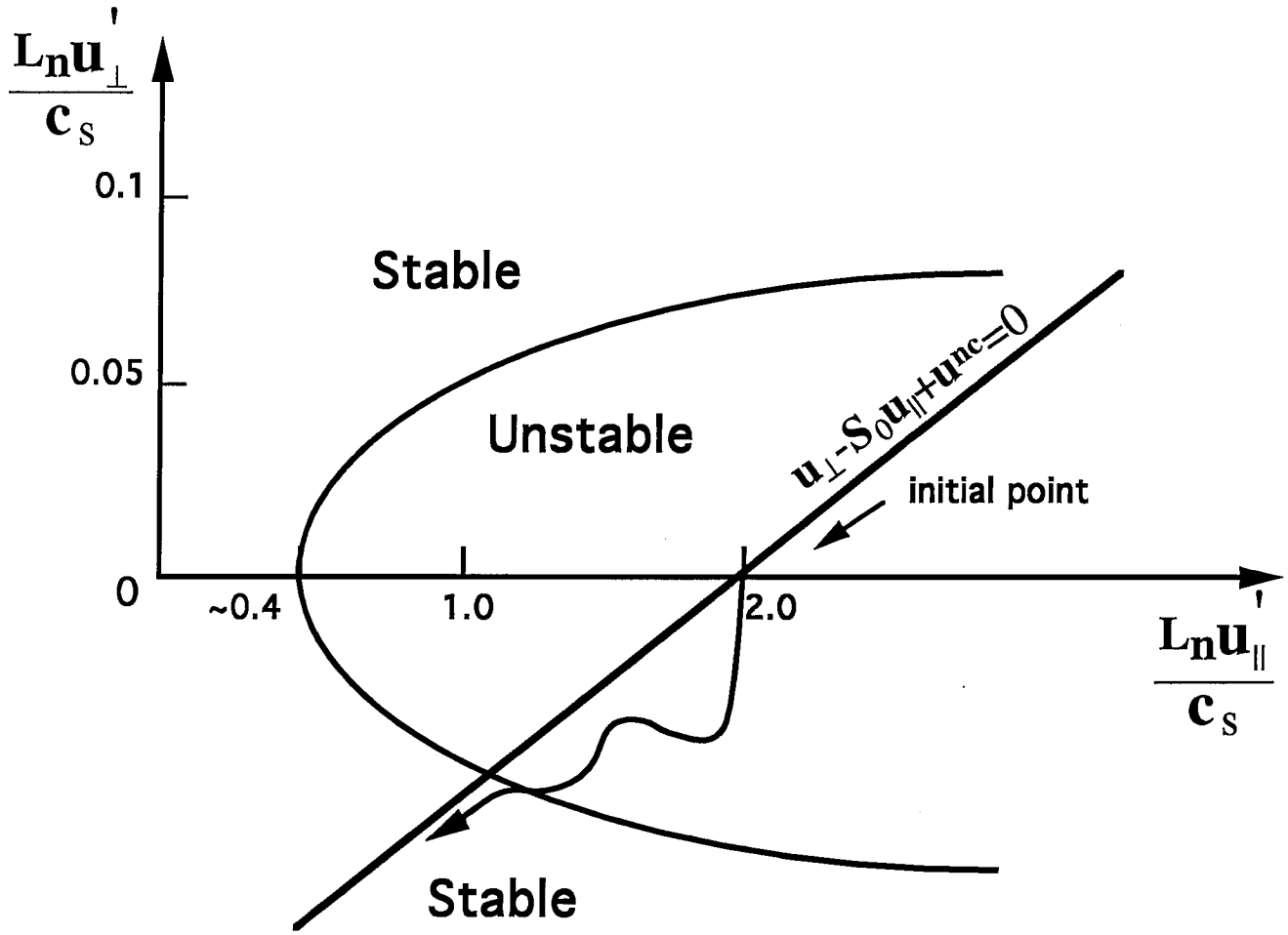

Figure 14

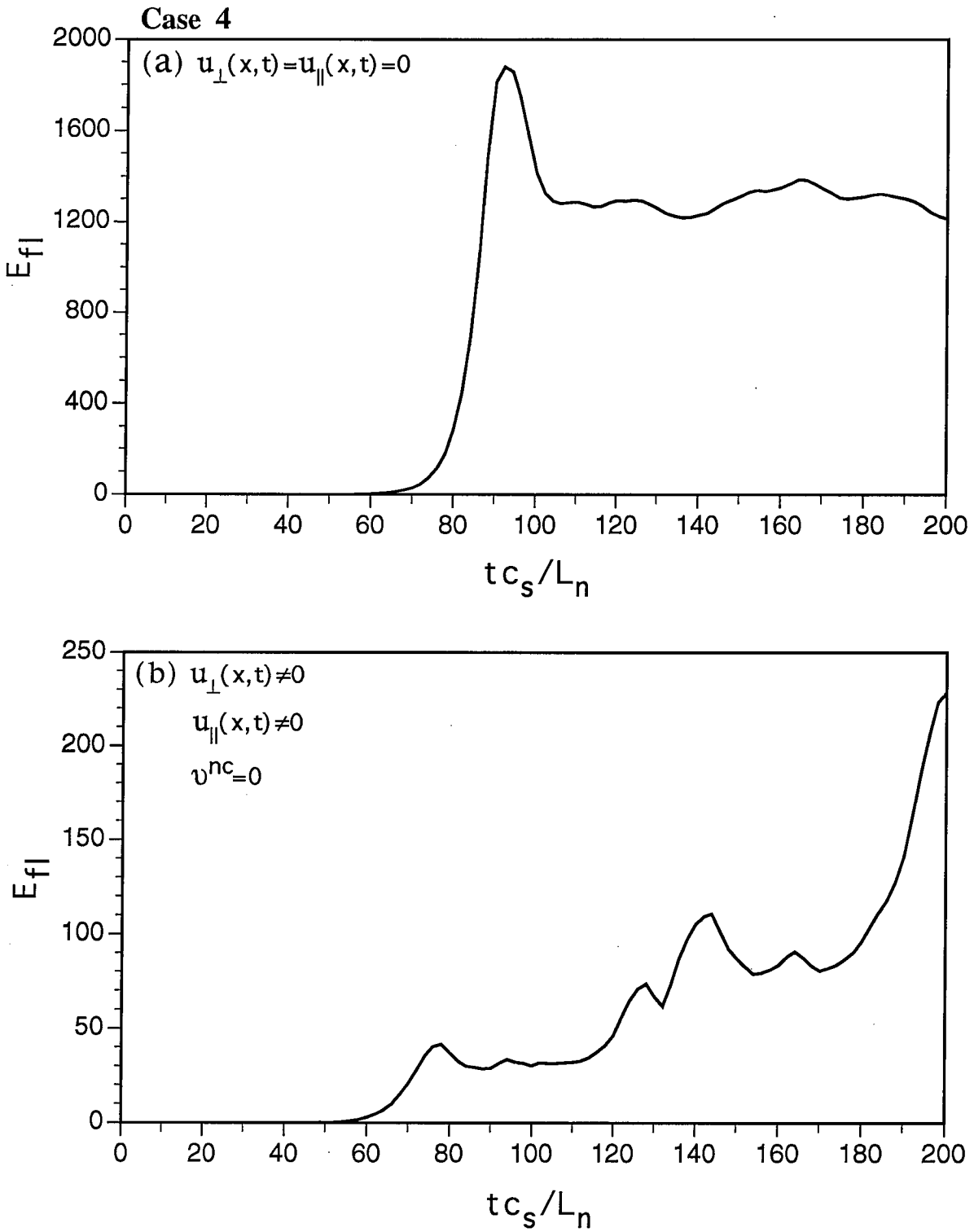
Case 4
(a) $u_\perp(x,t)=u_\parallel(x,t)=0$
E_{fl}
tc_s/L_n
(b) $u_\perp(x,t)\neq 0$
$u_\parallel(x,t)\neq 0$
$v^{nc}=0$
E_{fl}
tc_s/L_n

Figure 15

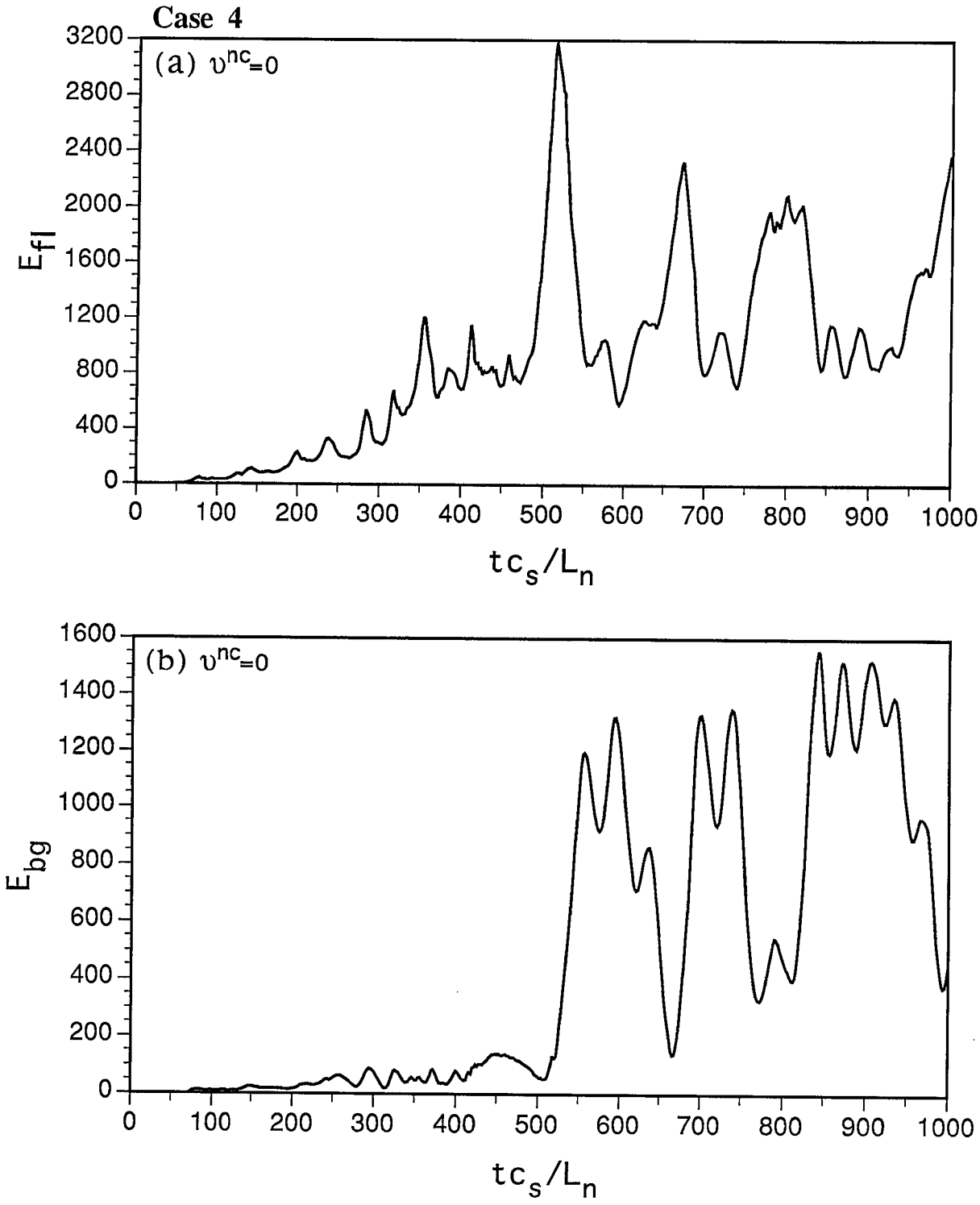
Case 4
(a) $\upsilon^{nc}=0$
E_{fl}
3200
2800
2400
2000
1600
1200
800
400
0
0
100
200
300
400
500
600
700
800
900
1000
tc_s/L_n
(b) $\upsilon^{nc}=0$
E_{bg}
1600
1400
1200
1000
800
600
400
200
0
0
100
200
300
400
500
600
700
800
900
1000
tc_s/L_n

Figure 16

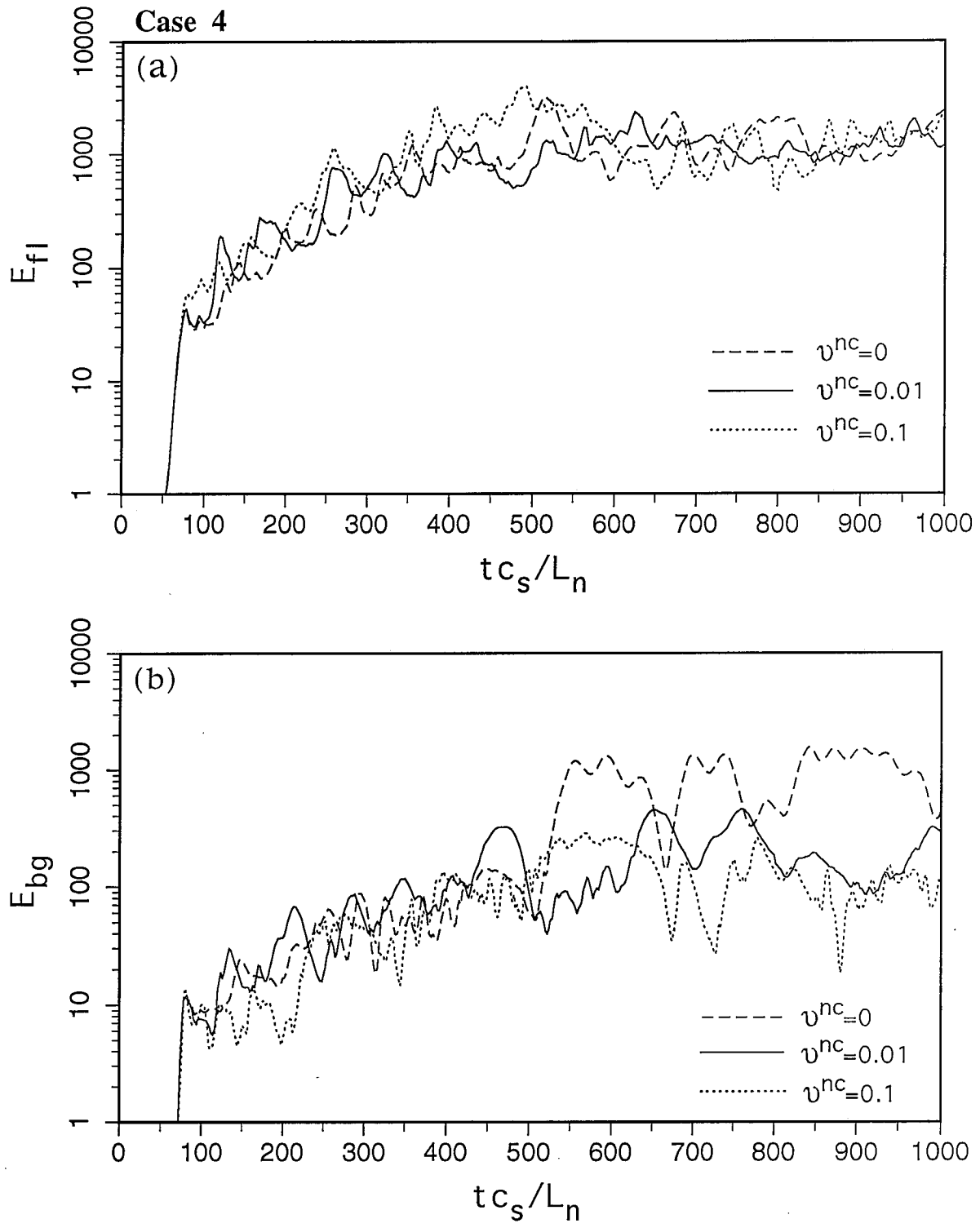
Case 4
(a)
E_{fl}
1
10
100
1000
10000
0
100
200
300
400
500
600
700
800
900
1000
tc_s/L_n
υ^{nc}=0
υ^{nc}=0.01
υ^{nc}=0.1
(b)
E_{bg}
1
10
100
1000
10000
0
100
200
300
400
500
600
700
800
900
1000
tc_s/L_n
υ^{nc}=0
υ^{nc}=0.01
υ^{nc}=0.1

Figure 17